Universität Potsdam

Institut für Physik und Astronomie

Master Thesis

in Astrophysics

The role of galaxy environment in the formation of multiple stellar populations in globular clusters

Candidate:	Viswajith Vanaraj, B.Sc.
Mat.Nr.:	794475
Supervisor 1:	Prof. Dr. Maria-Rosa Cioni
Supervisor 2:	Dr. Florian Niederhofer
Research site:	Leibniz-Institut für Astrophysik
Examiner 1:	Prof. Dr. Maria-Rosa Cioni
Examiner 2:	Prof. Dr. Matthias Steinmetz
Submission date:	02.03.2023

This thesis is based on Vanaraj et al. (2021). I take this thesis as an opportunity to introduce and elaborate on the research background our study builds upon. As in Vanaraj et al. (2021), I have used the collective pronoun 'we' instead of the singular pronoun 'I' throughout this thesis. The contributions of my co-authors to Vanaraj et al. (2021) are as follows:

Dr. Florian Niederhofer helped kickstart my research by providing me with the parameter file template for DOLPHOT and the Python script to eliminate field stars. He was also my supervisor and provided constructive comments and suggestions to help improve my manuscript.

Dr. Paul Goudfrooij calculated the initial masses of NGC 1786 and NGC 1898 used in the study.

I hereby declare that this thesis is the product of my own work. All the assistance received in preparing this thesis and the sources used have been acknowledged. No part of this thesis has been submitted elsewhere for any other degree.

(Signature)

"Cultivation of mind should be the ultimate aim of human existence."

– Annal Dr.B.R.Ambedkar

First of all, I would like to thank my parents, Krishnaveni and Vanaraj, for striving hard to get an education for themselves in an era when it was still not a common occurrence for people like us and hence paved way for me to develop an inner sense of value to seek knowledge. I would also like to thank them and my sister Kaaviya for providing much needed financial support during my studies.

I would like to wholeheartedly thank Dr. Florian Niederhofer for guiding, supporting and encouraging me every step of the way. It would take an entire thesis to describe how good of a supervisor he is. Though I always suspected that I would love research, I didn't expect it to have a therapeutic effect on me. Dr. Niederhofer was the primary reason behind that nurturing research environment. He always treated me as a colleague instead of as a student which, in no uncertain terms, was a great morale boost personally. I hope that he continues to teach and supervise students for the sake of the student community.

I would like to thank Prof. Dr. Maria-Rosa Cioni for giving me the opportunity to be a part of the wonderful 'Dwarf Galaxy and Galactic Halo' section and its members from whom I have learnt a lot. I would like to thank Dalal El-Youssoufi for her tips and suggestions for my PhD hunt. I would also like to thank the members of 'Milky Way and the Local Volume' section for their contributions in the joint group meetings. Especially, I would like to thank Dr. In Sung Jang for his help with DOLPHOT and his personal note congratulating me when I published my paper. I would also like to thank Prof. Dr. Matthias Steinmetz for agreeing to be an examiner of my thesis despite his very busy schedule.

I would like to thank my friend Vigneshwaran, conversations with whom have always helped me clear my mind and put me at ease. I would like to thank my friends Syed Aslam Ahmed and Mohammad Hossain for the delicious meals they have cooked for me over the course of my Master studies. I would like to thank Jeicot Delgado for offering me food he brought back from his workplace on several occasions. I would also like to thank Rashme, Preeti and Aadhavan for being wonderful texting buddies during the pandemic and help beat the isolation. This thesis makes use of Jan Brennenstuhl's LaTeX template.

Zusammenfassung

Kugelsternhaufen bestehen nicht, wie lange Zeit vermutet, aus einer einzelnen Sternpopulation, sondern beherbergen Sterne mit einem unterschiedlichen Gehalt an leichten chemischen Elementen. Auch nach Jahrzehnten der Forschung bleibt es ein Rätsel wie sich diese unterschiedlichen Sternpopulationen in Kugelsternhaufen gebildet haben. Dabei bleibt auch die Frage, ob die Umgebung der Heimatgalaxie bei der Entstehung eine Rolle spielt, unbeantwortet. In dieser Arbeit analysieren wir Aufnahmen des Hubble-Weltraumteleskops von NGC 1786 und NGC 1898, zwei klassischen (älter als 10 Milliarden Jahre) Kugelsternhaufen in der Großen Magellanschen Wolke. Das Ziel dieser Analyse ist es, diese mit Kugelsternhaufen in unserer Galaxie zu vergleichen um zu bestimmen ob es systematische Unterschiede zwischen den Sternhaufen gibt, bezüglich der chemischen Zusammensetzung der verschiedenen Sternpopulationen innerhalb eines Sternhaufens. Wir berechneten die Breite des Roten Riesenastes der beiden Kugelsternhaufen, unter Berücksichtigung des Effekts der Metallizität der Sterne. Die gemessenen Breite in einer speziellen Kombination von optischen und ultravioletten Filtern lässt direkte Rückschlüsse auf die Verteilung der Elementhäufigkeit unter den Sternen zu. Wir verglichen unsere Werte mit verfügbaren Daten von Kugelsternhaufen in der Milchstraße, als Funktion der Anfangsmasse und der gegenwärtigen Masse der Sternhaufen. Unsere Ergebnisse zeigen, dass NGC 1786 und NGC 1898 dem selben allgemeinen Trend folgen, welcher von Kugelsternhaufen der Milchstraße definiert wird. Sternhaufen welche sich nun in der Milchstraße befinden, jedoch vermutlich aus verschiedenen Vorläufergalaxien stammen, folgen darüber hinaus ebenfalls dem selben Trend. Unsere Ergebnisse deuten darauf hin, dass die Umgebung der Heimatgalaxie bei der Entstehung mehrerer Sternpopulationen in Kugelsternhaufen nur eine geringe Rolle spielt.

Abstract

Globular clusters are not composed of a homogenous star population as previously thought. They host distinct star populations, termed as 'Multiple Stellar Populations' or 'Multiple Populations', that differ in their quantity of light elements. Even after decades of research, the origin of such populations in globular clusters remains enigmatic. The question as to whether the galaxy environment plays a role in their formation remains unanswered. To that extent, we analyzed two classical (older than 10 billion years) Large Magellanic Cloud globular clusters namely, NGC 1786 and NGC 1898, using imaging data from *Hubble Space Telescope* to compare and contrast them with ancient Milky Way globular clusters to assess systematic differences that might exist between their abundance variations. The width of the Red Giant Branch in the U, B and I bands is a direct proxy of Carbon, Nitrogen and Helium abundances within a cluster. We calculated their Red Giant Branch width, subtracted the effect of metallicity and compared it with the available data on Milky Way globular clusters by plotting them against initial and current cluster mass. We see that the two clusters follow the same general trend as that of Milky Way globular clusters. We also see that Milky Way globular clusters from different progenitors follow the same general trend as one another, indicating that the galaxy environment may only play a minor role in the formation of multiple populations within globular clusters.

Contents

List of abbreviations

1G First Generation
2G Second Generation

ACS Advanced Camera for Surveys
AGB Asymptotic Giant Branch
AS Artificial Star

ChM Chromosome Map
CMD Colour-Magnitude Diagram
CTE Charge Transfer Efficiency

DR Differential Reddening

EDR3 Early Data Release 3
ERS Early Release Science

FITS Flexible Image Transport System
FRMS Fast Rotating Massive Stars

GC Globular Cluster
GO General Observer

HST Hubble Space Telescope

IOM Integrals of Motion

JWST James Webb Space Telescope

LMC Large Magellanic Cloud

MC Magellanic Cloud
ML Mass Loss
MLA Mass Loss per Gyr
MLF Mass Loss Fraction
MP Multiple Population
MS Main Sequence
MSTO Main Sequence Turn-Off
MW Milky Way

NIR Near Infrared
NIRCAM Near Infrared Camera

OC Open Cluster

PAM Pixel Area Map
PSF Point Spread Function

RGB Red Giant Branch

S/N Signal to Noise Ratio
SAA South Atlantic Anomaly
SMC Small Magellanic Cloud
SNe Supernovae explosions
SSP Simple Stellar Population

UV Ultraviolet
UVIS Ultraviolet and Visible

WCS World Coordinate System
WFC Wide Field Camera
WFC3 Wide Field Camera 3

List of Figures

List of Tables

Chapter 1

Introduction

Star clusters are broadly classified into two types: Globular Clusters (GCs) and Open Clusters (OCs). The term *globular cluster* was coined by William Herschel in his famous *Catalogue of Nebulae and Clusters of Stars* (Herschel 1789). GCs are roughly spherical, gravitationally bound star cluster systems with thousands of stars while OCs have only a few hundred stars at the most which are dispersed. GC stars are mostly coeval and hence have roughly the same age. Since they are gravitationally stable, they can exist for billions of years, unlike OCs which typically disintegrate after a few million years. GCs have been proposed as possible sites for the existence of spacefaring civilizations due to the existence of stable habitable zones that can exist for many Hubble times and high star densities enabling interstellar travel (Di Stefano & Ray 2016). GCs are used to test stellar evolution models (Salaris 2013). Due to their long life span, comparable to the age of their host galaxy, they serve as natural laboratories to study galaxy formation and evolution. One of the interesting insights in recent years is that most of the Milky Way (MW) GCs were formed when less than 10 % of the MW stellar mass had been formed, shedding some much needed light on the early MW formation (Dotter et al. 2010; Madau & Dickinson 2014). Chemical composition of GCs have also served as indications of galaxy merger events (Lee et al. 1999). Age estimates of GCs have been used to determine that the age of the universe is about 13.5 Gyr, consistent with the findings of the Planck mission assuming the Lambda−Cold Dark Matter cosmological model (Valcin et al. 2020, 2021). Hence, it is apparent that studying GCs has implications ranging from extraterrestrial life to the origin of our universe itself.

Figure 1.1: Absorption spectrum obtained by Popper (1947) showing a break around the 4215 line of 9 Pegasi (supergiant), M 13 − 194 and ß Herculis each. M 13 − 194 refers to a giant star in Messier 13. On the right side, spectral types (G5) and luminosity classes (Ib, III) are mentioned.

1.1 What are 'Multiple Populations'?

Until less than a few decades ago, GCs were considered to be 'Simple Stellar Populations' (SSPs), that is, stellar populations with similar age and chemical composition. Chemical inhomogeneities among stars in globular clusters have been known to exist for nearly a century. Using a slitless prism spectrogram, Lindblad (1922) observed that giant K0 stars in Messier 13 had weak CN absorption lines in the UV and blue bands relative to other stars in the cluster. Popper (1947) performed spectroscopic observations and found that there is a break in the continuum around 4215 line (corresponding to CN) in the absorption spectrum of giants in Messier 13 (see Figure 1.1), thereby confirming the result of Lindblad (1922) that GC giants have abnormal CN absorption. He also found that the break is weak compared to supergiants (see Figure 1.1) and that there is a difference between CN absorption in GC giants and standard stars of the same luminosity class. He found that one particular giant had a CN band strength equivalent to luminosity class of II or III when most other giants were fainter, providing definite evidence of abundance variation among giant stars.

In the last few decades, huge strides made in astronomical instrumenta-

tion have enabled us to study these inhomogeneities in great depth using spectroscopy and photometry. It has revealed significant star-to-star abundance variations in light elements such as C, N, Na, O, Al and Mg which have laid to rest the traditional assumption that GCs were SSPs. The inhomogeneities are not random but exhibit certain (anti-)correlations in light elements such as N-C, Na-O and sometimes Al-Mg (anti-)correlations (Carretta et al. 2009, 2015). These star-to-star variations are not accounted for by standard nucleosynthetic processes. This phenomenon is known as 'Multiple Populations' (MPs) (see Bastian & Lardo 2018 and Milone & Marino 2022 for a review). Popper (1947) is generally accepted to be the first definitive evidence of chemical abundance variation in a GC and thereby, the first definitive detection of an MP though this assertion has been disputed (Smith & Briley 2006).

1.2 Basic Properties of Multiple Populations

A defining feature of GCs with MPs is that they host two stellar populations: the primordial population or first generation (1G) which consists of stars with a similar chemical composition as that of field stars with the same metallicity and the secondary population or second generation (2G) which consists of stars enhanced or depleted in certain elements exhibiting the above mentioned anti-correlations with respect to the primordial population. 2G stars are also found to be enriched in Helium (Lagioia et al. 2018; Milone et al. 2018; Zennaro et al. 2019). Some clusters additionally host an extended primordial population indicating Fe abundance variations and the presence of binary systems within that population (Milone et al. 2015; D'Antona et al. 2016a; Marino et al. 2019). MPs have been detected across evolutionary stages from main sequence (MS) to white dwarfs (Milone et al. 2012b, c; Bellini et al. 2013; Piotto et al. 2015; Milone et al. 2017). In most GCs, 2G stars outnumber 1G stars with the ratio correlated with the mass of the cluster (Milone et al. 2017; Dondoglio et al. 2021). There is usually no observed Fe spread or Fe-peak element spread between the populations (Carretta et al. 2009) though there are exceptions to this rule (Yong et al. 2013; Marino et al. 2015, 2019). GCs also host discrete sub-populations within the 2G population (Milone et al. 2017).

MPs seem to be an inherent property of classical (older than 10 Gyr)

Galactic[1] GCs though there are numerous exceptions (Milone et al. 2014; Salinas & Strader 2015; Dotter et al. 2018; Milone et al. 2020). These are mostly low-mass clusters, suggesting that cluster mass is an important parameter in the formation of MPs. Similar abundance variations have also been found in classical extragalactic GCs within Fornax dwarf spheroidal galaxy (Larsen et al. 2014), Large Magellanic Cloud (LMC) (Mucciarelli et al. 2009; Gilligan et al. 2019) and Small Magellanic Cloud (SMC) (Dalessandro et al. 2016; Niederhofer et al. 2017a). So, MPs were thought to be exclusive to classical GCs. But recently, MPs have also been detected in intermediate age GCs (2-6 Gyr) in Magellanic Clouds (MCs, Hollyhead et al. 2017; Niederhofer et al. 2017b). NGC 1783 is the youngest GC ($\sim$1.5 Gyr) with evident presence of MPs (Cadelano et al. 2022).

1.3 Photometric Diagrams

Until the recent decades, spectroscopy was the popular choice to detect MPs. But photometry has also proven to be a reliable tool to detect the presence of MPs albeit dependent on spectroscopy since spectral abundances are required to determine which photometric bands are required to disentangle stars with different abundances. Photometry has the advantage over spectroscopy that much more stars can be analyzed simultaneously which makes it a powerful tool. There are quite a few types of photometric diagrams that aid in the detection of MPs. We look at a couple of types here.

1.3.1 (Pseudo-)Colour-Magnitude Diagrams

Colour-magnitude diagram (CMD) splits the two populations based on abundance variations depending on the filters used. Filters sensitive to molecular bands corresponding to C, N, Na, O, Al and Mg will be able to discriminate between the two populations due to the underlying abundance variations in those elements. Marino et al. (2008) used U $-$ B vs U CMD to separate MPs with different abundances. As noted by them, stars with high N abundance were also high in elements Na and Al (and weak in C, O and Mg respectively). Such stars were classified as CN-strong (since CN acts as a proxy for N abundance) stars and those weak in N, Na and Al (and strong in C, O and Mg) were classified as CN-weak stars. Since N absorption is

[1]The Milky Way is also referred to as 'the Galaxy' with a capital G.

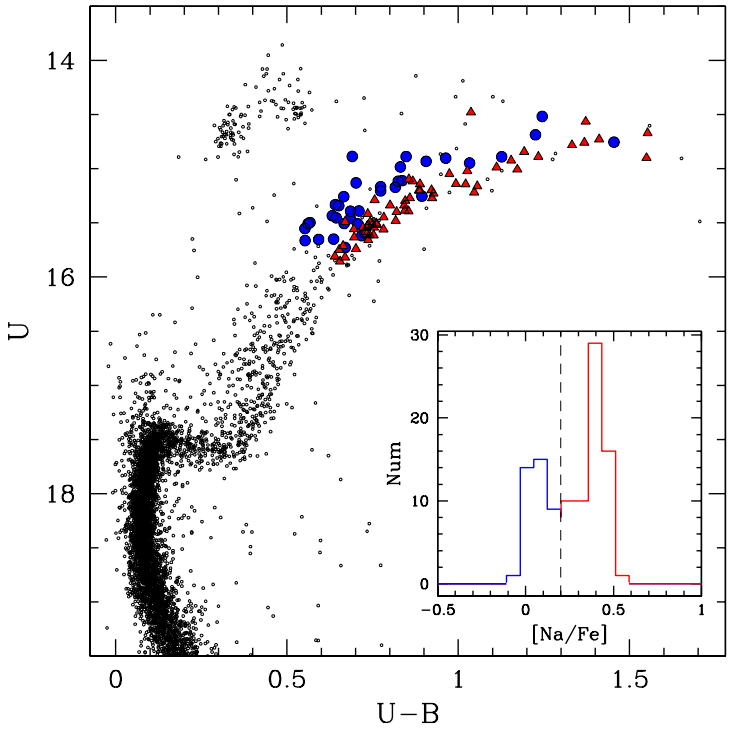

Figure 1.2: U − B vs U CMD of NGC 6121. Blue circles indicate stars with [Na/Fe] < 0.2 dex (1G) while red triangles indicate stars with [Na/Fe] > 0.2 dex (2G). Picture adapted from Marino et al. (2008).

relatively strong in U band and relatively weak in B band, U and B band magnitudes are relatively brighter and fainter respectively for 1G stars and vice-versa for 2G stars. So, 1G stars will be pushed to the bluer side and 2G stars will be pushed to the redder side of the CMD. This is the advantage exploited in photometric diagrams to disentangle and study the different populations within a cluster. Figure 1.2 shows the U − B vs U CMD of NGC 6121 with the two populations distinguished based on Na abundance variations.

Not only CMDs, pseudo-CMDs have also been used to separate the two populations. Pseudo-colour $C_{X,Y,Z}$ is defined as $(m_X - m_Y) - (m_Y - m_Z)$. $C_{F336W,F438W,F343N}$ is the pseudo-colour in the Ultraviolet and Visible (UVIS) channel filters F336W, F438W and F343N of the Wide Field Camera 3 (WFC3) in Hubble Space Telescope (HST). $C_{F336W,F438W,F343N}$ is useful to identify MPs with different C and N abundances due to the presence of strong NH absorption lines in F336W and F343N filters and CH absorption

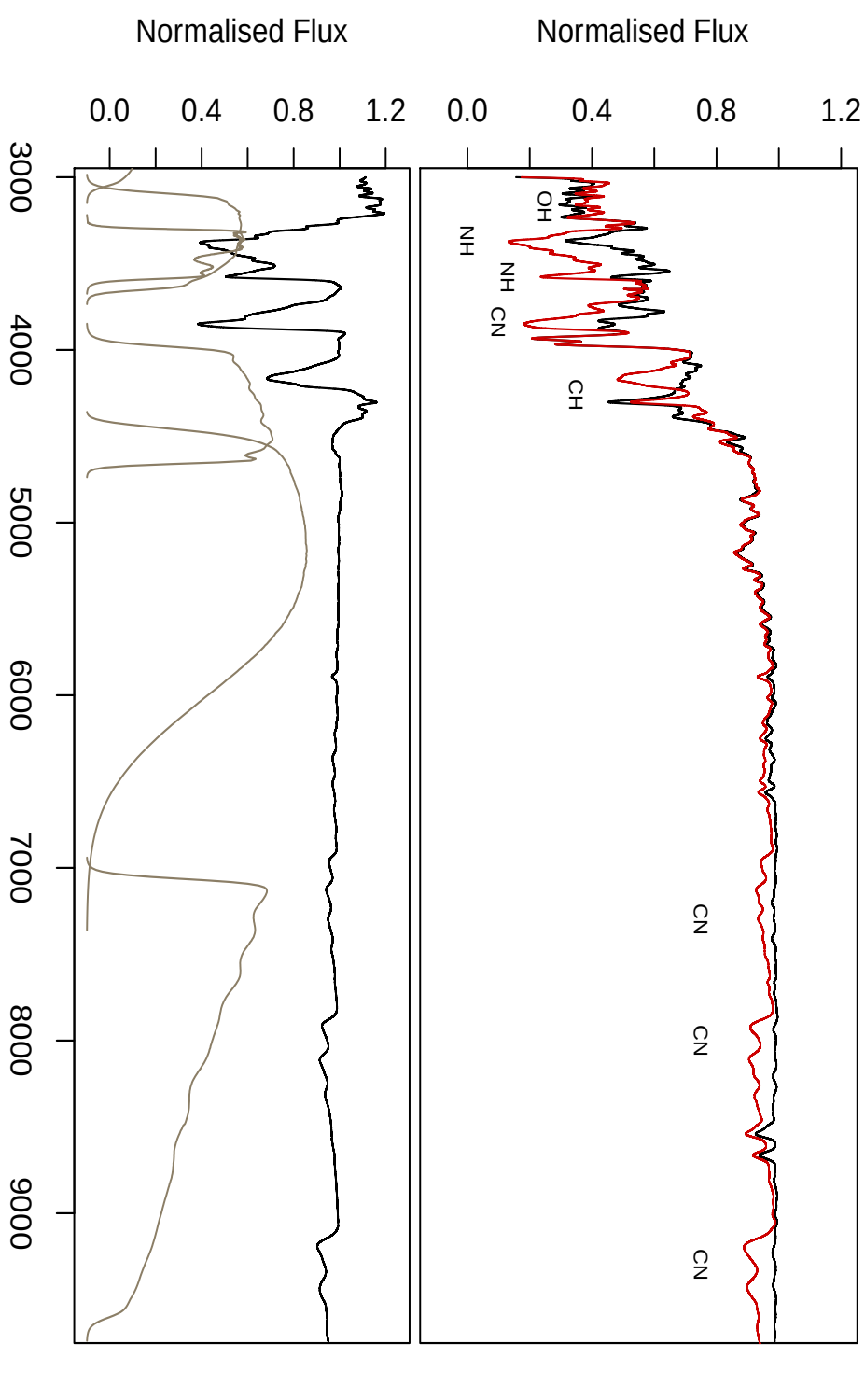

Figure 1.3: *(a)*: Normalized synthetic absorption spectra of RGB stars with 1G (black) and 2G (red) populations. Various absorption bands that vary between the two populations are marked. *(b)*: Flux ratio (black) between 1G and 2G spectra along with various HST WFC3/UVIS filters (gray). From left to right: F336W, F343N, F438W, F555W and F814W filters. Picture adapted from Bastian & Lardo (2018).

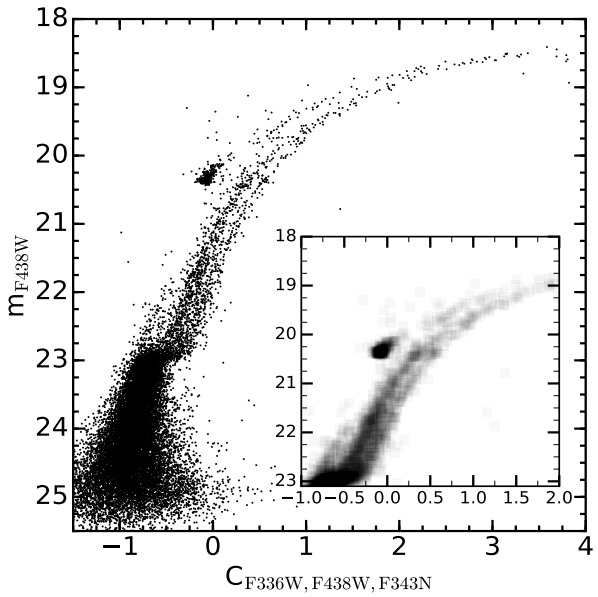

Figure 1.4: $C_{F336W,F438W,F343N}$ vs m_{F438W} CMD of NGC 121. The inner panel shows the Hess diagram zoomed into the RGB region where the split between the two populations is evident. Picture adapted from Niederhofer et al. (2017a).

features in F438W filter (Marino et al. 2008; Yong et al. 2008; Milone et al. 2012a, 2013; Piotto et al. 2015; Niederhofer et al. 2017a, b). F336W and F438W are analogous to broadbands U and B in Johnson-Cousins respectively while F343N corresponds to narrow U band. In Figure 1.3, panel (a) shows the normalized synthetic spectra of 1G and 2G Red Giant Branch (RGB) stars with absorption bands of OH, NH, CN and CH. OH acts a proxy for O, NH and CN for N and CH for C. Panel (b) shows the ratio of normalized flux between 1G and 2G stars and various HST bands. We can see that there is a strong NH absorption in F336W and F343N filters and a strong CH absorption in F438 filter. So, 1G stars (C-rich but N-poor) appear relatively bright in F336W and F343N filters but relatively faint in F438W filter. It is vice-versa for 2G stars (C-poor but N-rich).

To illustrate this technique, Figure 1.4 shows the $C_{F336W,F438W,F343N}$ vs m_{F438W} pseudo-CMD of NGC 121. The inner Hess diagram shows the visible split between the two populations in the RGB region. Variation in C+N+O sum causes split sequences in some filters (Pietrinferni et al. 2009) and hence can result in false detection of MPs. As noted by Pietrinferni et al. (2009), large colour spreads are observed in RGB even with constant C+N+O sum.

Hence the correlation of RGB width with the global parameters (metallicity, mass, age etc.) is a useful tool to understand the phenomenology of MPs. The difference between RGB width observed in SSPs and MPs is that the observed spread in SSPs can be explained exclusively by observational errors.

Panel (a) of Figure 1.5 shows the pseudo-CMD of NGC 6752 while panel (b) shows some of the anti-correlations mentioned in section 1.1. Figure 1.5 nicely illustrates the consistency between spectroscopic and photometric results. In this thesis, the pseudo-colour $C_{F336W,F438W,F814W}$ will be used to analyze the RGB of two old GCs in the LMC. F814W is analogous to I band. This combination is effective in separating stars with different C/N and He content since $m_{F336W} - m_{F438W}$ is sensitive to C and N and $m_{F438W} - m_{F814W}$ is sensitive to He content.

1.3.2 (Pseudo-)Colour-Colour diagrams

Over the last ten years, colour-colour diagrams have also been used to detect and characterize MPs, especially along the main sequence phase (Milone et al. 2012b). Figure 1.6 shows the $(m_{F336W} - m_{F435W})$ vs $(m_{F275W} - m_{F336W})$ colour-colour diagram of MS stars in 47 Tuc. The right panel shows the clear delineation between 1G and 2G stars. It illustrates that the populations are discrete and the predominance of 2G stars over 1G stars.

Over the past 5 years, pseudo-two-colour diagram or 'Chromosome Map' (ChM) has also been used to detect MPs (Milone et al. 2017). The difference between a standard colour-colour diagram and a ChM is that both the axes are verticalized in the latter such that each population is grouped in a small region of ChM. Figure 1.7 shows $\Delta_{\rm F275W,F814W}$ vs $\Delta_{C\rm F275W,F343N,F435W}$ ChM for 47 Tuc which correspond to the normalized $m_{\rm F275W} - m_{\rm F814W}$ colour and $C_{\rm F275W,F336W,F438W}$ pseudo-colour respectively in the indicated filter combinations. $m_{\rm F275W} - m_{\rm F814W}$ is sensitive to He variations while $C_{\rm F275W,F336W,F438W}$ is sensitive to N variations. The left panel of Figure 1.7 shows the ChM of RGB and AGB (Asymptotic Giant Branch) stars while the right panel shows the ChM of MS stars. The clustered group on the top is the 2G population while the less numerous bottom group is the 1G population. The separation dynamic between the two populations in the ChM seems consistent across the considered stellar evolutionary stages. We can see that the 1G population has a non-zero slope which may point to marginal N variations among the 1G stars.

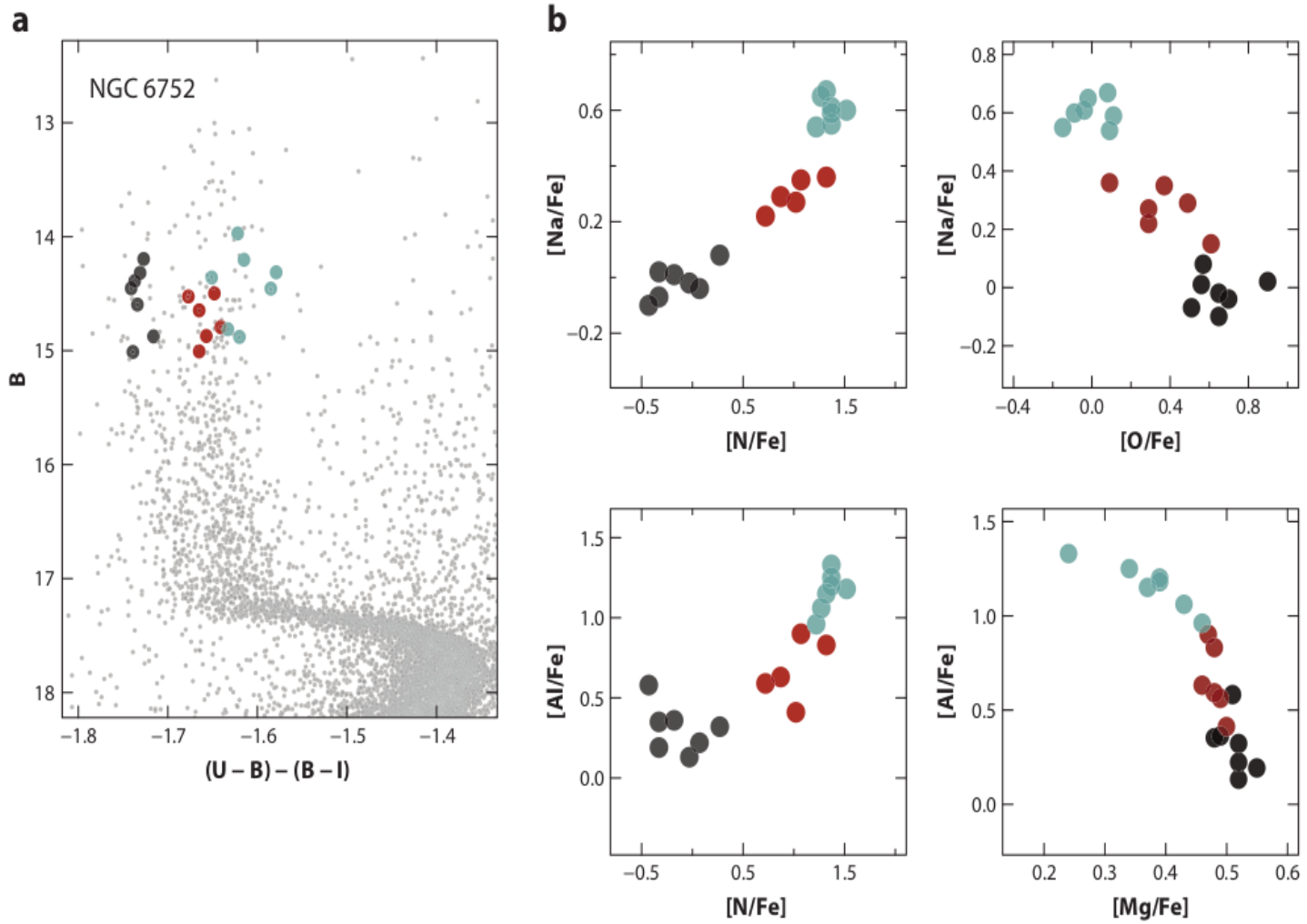

Figure 1.5: *(a)*: Pseudo-CMD of NGC 6752. Different colours of highlighted stars correspond to different Na content. *(b)*: Light abundance variations of highlighted stars in *(a)*. Adapted from Bastian & Lardo (2018).

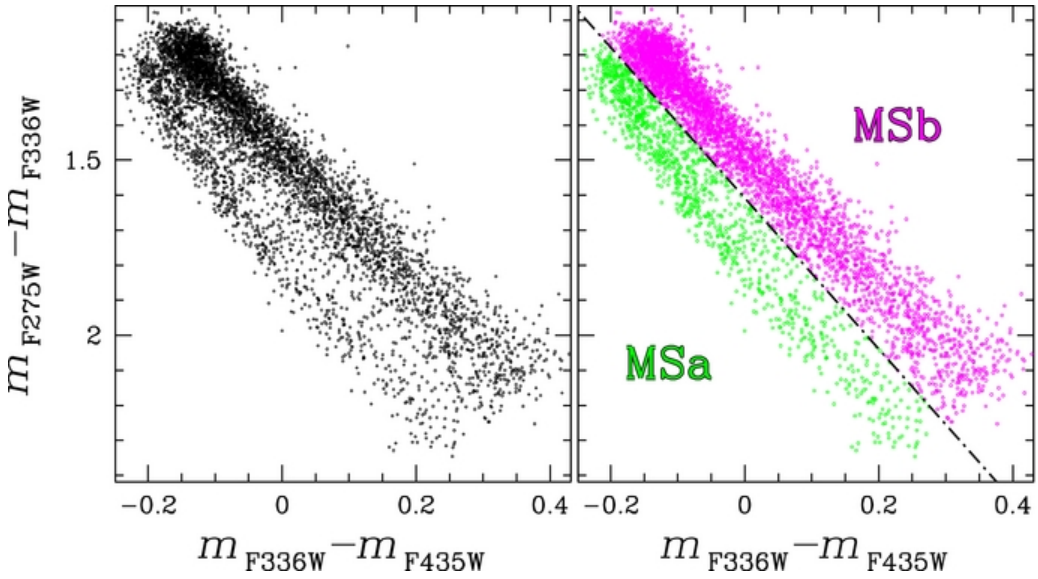

Figure 1.6: $(m_{F336W} - m_{F435W})$ vs $(m_{F275W} - m_{F336W})$ plot of MS phase in 47 Tuc. The dashed line in the right panel separates the 1G (MSa) and the 2G (MSb) populations. Figure adapted from Milone et al. (2012b).

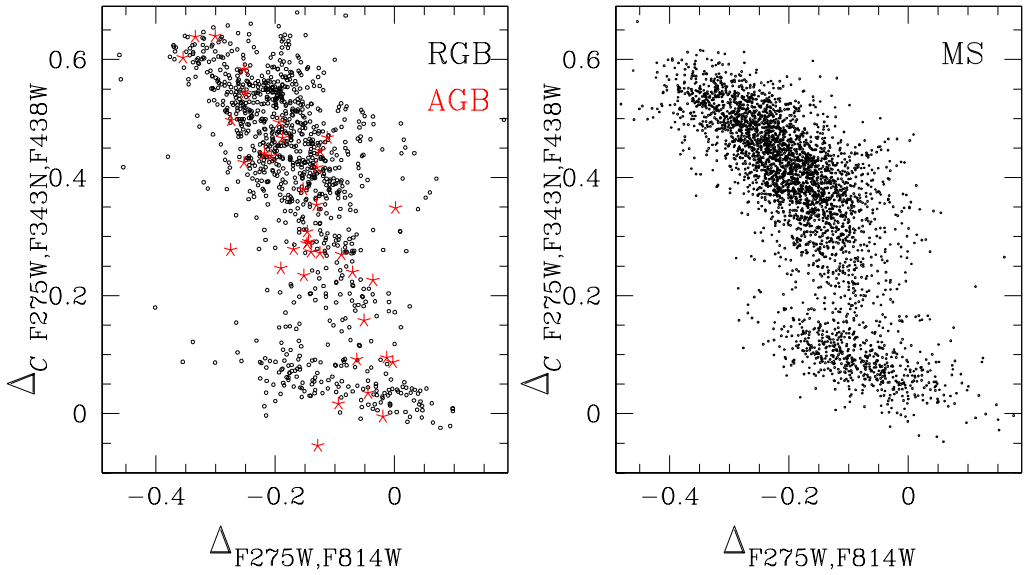

Figure 1.7: $\Delta_{F275W,F814W}$ vs $\Delta_{CF275W,F343N,F435W}$ ChM of 47 Tuc. Figure adapted from Milone & Marino (2022).

1.4 Impact of various parameters on MPs

Though much progress has been made in the study of MPs in the last two decades, their origin remains enigmatic. To understand the origin and formation of MPs, we need to know the impact of various parameters (e.g. age, mass, environment etc.) on their manifestation. Milone et al. (2017) analyzed 57 Galactic GCs from the *HST UV legacy survey* (Piotto et al. 2015) and the correlation of their RGB width with various global GC parameters. The RGB width was calculated in the colour $m_{F275W} - m_{F814W}$ and in the pseudo-colour $C_{F275W,F336W,F438W}$. It was found that the intrinsic RGB width correlates with metallicity and after removing the dependence on metallicity, significant correlations between RGB width and mass and luminosity were observed. The role of age and galaxy environment could not be discerned since the sample was restricted to classical Galactic GCs older than 11 Gyr (Dotter et al. 2010).

Lagioia et al. (2019a) analyzed the above sample along with additional Galactic and extragalactic GCs. The RGB width was calculated in the pseudo-colour $C_{F336W,F438W,F814W}$. As noted by them, there is a large number of observations in these bands, in the archives of both HST and ground-based telescopes. Furthermore, this combination of filters requires significantly lesser observation time[2] than the one used by Milone et al. (2017) with the same S/N ratio due to the fast decline of UV flux in the RGB stars and the low transmittance of F275W filter (see Figure 1.8). It enables us to observe distant clusters with lesser difficulties. It was found that there was no correlation between the intrinsic RGB width and the age of the cluster while there was a significant correlation between the intrinsic RGB width and the mass of the cluster. They also found that the intrinsic RGB width and the metallicity subtracted RGB width (which they call the 'normalized' RGB width) of extragalactic GCs is systematically lower than that of Galactic GCs. It indicates that MC GCs might have smaller internal light element abundance variations than Galactic GCs. However, the 7 extragalactic GCs used by Lagioia et al. (2019a), with the exception of NGC 121, are much younger than Galactic GCs. In order to learn about the role played by the host galaxy environment in the manifestation of MPs, we need to analyze extragalactic GCs in the same age range as that of Galactic GCs so that we can study the effect of their respective host galaxies. The aim of this thesis

[2]Observation time can be determined with the Exposure Time Calculator: https://etc.stsci.edu/etc/input/wfc3uvis/imaging/

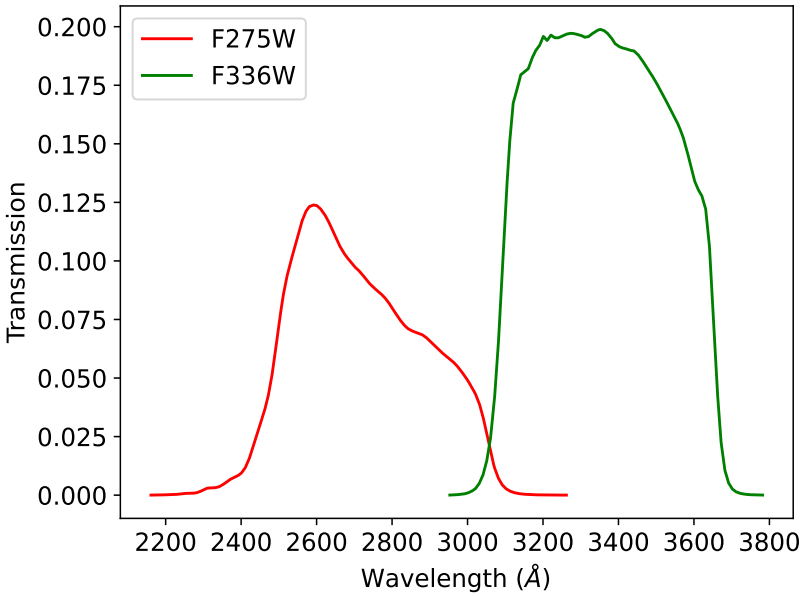

Figure 1.8: Transmission curves of F275W (red) and F336W (green) filters in WFC3/UVIS1 camera.

is to analyze two classical LMC GCs, namely, NGC 1898 and NGC 1786 and look at the correlation between their normalized RGB width in pseudo-colour $C_{F336W,F438W,F814W}$ and mass, compare them with Galactic GCs and see if they exhibit systematic abundance variations.

1.5 Why is exploring the role of galactic environment important?

A number of scenarios have been proposed to explain the formation of MPs though no particular scenario explains all the observational properties. The typical AGB scenario postulates that 2G stars are formed when ejecta from AGB stars in a cluster accumulate together with the metal-enriched feedback from earlier supernovae explosions (SNe) (Dantona et al. 1983; Ventura et al. 2001). As mentioned in Section 1.2, there are no observed Fe or Fe-peak element spread between the populations. Hence, supernovae are ruled out as a possible source of enrichment. D'Antona et al. (2016b) hypothesize, using the observational studies of NGC 2808, multiple star formation events

with ejecta from different generations of AGB stars mixing with different amounts of pristine gas from Type II and Type Ia SNe to account for the observed chemical composition. A general problem with the AGB model is that only stars with 5 to 9 $M_{\odot}$ that pass through the AGB phase are hot enough to produce the observed abundance spreads. Since they make up only 7% of 1G stars under the assumption of a typical initial mass function, the observed 1:2 ratio of 1G and 2G stars in a typical GC is unexplained by the AGB scenario as there wouldn't be enough 1G stars to provide the required amount of enrichment material for the formation of the observed number of 2G stars. The Fast Rotating Massive Stars (FMRSs) scenario hypothesizes that 2G stars are formed when ejection winds from almost fully mixed FRMSs pollute the intracluster medium (Decressin et al. 2007). Elmegreen (2017) puts forward a model of enrichment taking into account the higher gas density, pressure and turbulence in galaxies at high redshifts. The model assumes interactions among massive stars including massive binaries (de Mink et al. 2009; Bastian et al. 2013) leading to shedding of stellar envelopes and hence releasing the p-processed elements into the cluster gas cloud. Massive star interactions also lead to gas expulsions ejecting low mass 1G stars at a velocity greater than the escape velocity of the GC. This explains the observed population ratio of 1G and 2G stars. But observational studies of young massive clusters don't support the idea of such an expulsion (Longmore 2015).

To better constrain the theoretical models, we require observational data directly related with the apriori assumptions about various parameters in the models. To know which models to further, reject or modify, those assumptions must be validated with empirical data. Scenarios like Elmegreen (2017) are built upon the assumption of a significant role played by the environment of the GC's host galaxy. Hence, this thesis aims to determine whether or not galactic environment plays an important role in the formation of MPs.

1.6 PSF photometry

1.6.1 Modelling of Point Spread Function

Point Spread Function (PSF) describes how a point light source is affected to distribute the incoming light across the telescope detector causing it to appear extended rather than point-like. It is determined by various instrumental (for example, diffractions and aberrations within the instrument)

and environmental (atmospheric conditions for ground-based observatories) factors. As Heasley (1999) points out, PSF-fitting photometry rests on two assumptions: all the imaged point-source targets can be represented by a PSF and the response of the detector is linear to the incoming light. Usually bright, isolated stars which are mostly free of starlight contamination in the detector frame are used to model the PSF (see Section 1.6.2). This is necessary to prevent the overestimation of the extended profile of a point source in crowded fields. There are three common methods to model PSF for HST images:

1) using Principle Component Analysis (Jarvis & Jain 2004)

2) estimating the amount of starlight that will fall on each pixel in the detector using observational data (Anderson & King 2000).

3) determining the instrumental effects and using them to model the spread of starlight on the detector. This method cannot be comprehensive for ground-based telescopes since atmospheric effects play a significant role in the determination of the PSF.

For HST images, the last method is predominantly used. In particular, for the last three decades, a method known as Tiny Tim has been used extensively to simulate PSFs for HST cameras (Krist 1993; Hook & Stoehr 2008; Krist et al. 2011). Tiny Tim raytraces the light from the instrument optics, acccounted for obscurations and aberrations, onto the entrance pupil of the cameras. It assumes that diffraction happens in a 2D plane since 3D effects due to Fresnel diffraction on PSF accuracy are small compared to unknown or poorly known parameters. It propagates the wavefront to focus using a Fast Fourier Transform. The modulus square of the resultant electric field is then used to produce the PSF. Tiny Tim also accounts for defocus due to time dependent changes, polishing errors and pixelization (image blurring). For ACS (Advanced Camera for Surveys) and WFC3 cameras of HST, Tiny Tim also accounts for geometric distortion. It has been used to process HST images for purposes including (but not limited to) measuring the size of globular clusters (Whitmore et al. 1999), galaxies (van Dokkum et al. 2008) and gravitational lensing observations (Leauthaud et al. 2007). Figure 1.9 shows a Tiny Tim PSF of F336W filter in WFC3/UVIS1 chip.

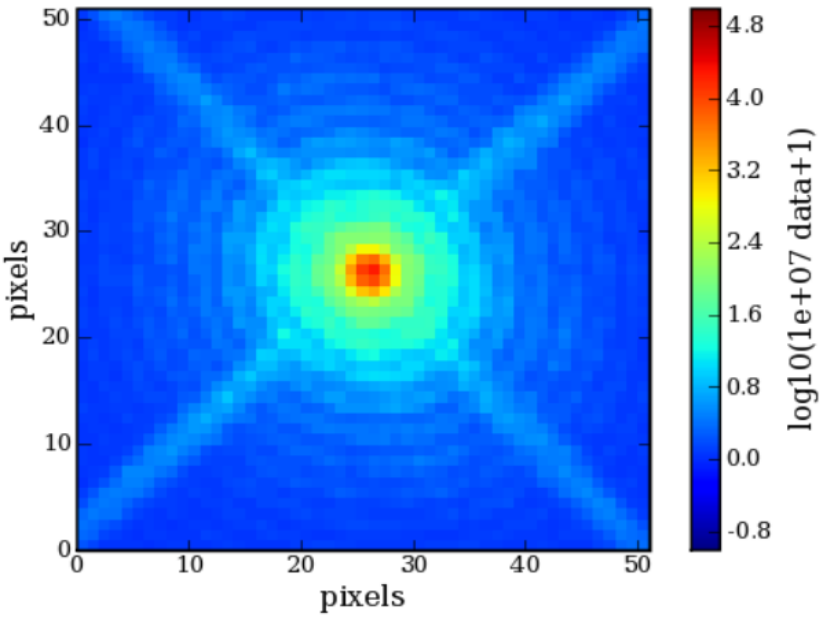

Figure 1.9: Tiny Tim PSF of WFC3/UVIS1 F336W filter. Image adapted from Hook & Stoehr (2008).

1.6.2 Performing photometry using DOLPHOT

DOLPHOT 2.0[3] (Dolphin 2000) is a pipeline used to perform photometry on HST images. It uses PSFs computed by Tiny Tim. Though precomputed PSFs are used, the exact shape of the PSF varies in each case. Magnitude detection of fainter stars depends on the shape of the PSF while that of the bright stars depends on the number of photon counts in the PSF. DOLPHOT fits the precomputed PSF to an observed image in a particular filter and deconvolves the point-source signal convolved with the PSF using an iterative algorithm to get the preliminary instrumental magnitude and brightness of the stars. After the first iteration, DOLPHOT calculates the PSF residuals to adjust for the specific focus and tracking conditions of the image under consideration. PSF residuals are calculated using stars that meet certain criteria based on sharpness, chi value, distance between the star and the edge of the usable chip area, pixel quality near the star and the brightness of its neighbours. The precomputed PSF and the PSF residuals are combined to get the new PSF. Then the iterations are continued till a convergence is

[3] http://americano.dolphinsim.com/dolphot/

reached, the convergence being defined as the best fit based on a chi-square based quality-of-fit parameter. After the convergence, a final photometry run is carried out to improve the accuracy of the determined star postions and brightnesses by computing PSF at any given point using linear interpolation. Then the process is repeated for the images in remaining filters followed by transforming the instrumental magnitudes to apparent magnitudes.

PSF photometry is preferred to aperture photometry in the detection of faint stars and in crowded fields. In aperture photometry, light from a point-source incident on the pixels in the aperture is summed up to determine the brightness. But uncertainties in the measurement of background sky level could result in dubious detections of supposed faint stars or miss the actual ones. In crowded fields, contamination from nearby stars becomes a problem in determining the flux of the source.

1.7 Thesis Overview

The purpose of this thesis is to determine whether galaxy environment plays a role in the formation of multiple stellar populations which are quantified by the width of RGB. We analyze two classical LMC GCs (NGC 1898 and NGC 1786), determine their RGB width in the HST WFC3/UVIS filters F336W, F438W and F814W and compare the results with the widths of other MC and Galactic GCs. This thesis is divided as follows:

In chapter 2, we describe the dataset and the photometric data analysis techniques. This includes the HST observations, data reduction using the photometric pipeline, selection of stars after performing photometry, artificial star tests, accounting for differential reddening and zero point variations and listing the cluster parameters used in this research.

In chapter 3, we explain the procedure to derive the intrinsic RGB width and the associated error of the GCs.

In chapter 4, we perform statistical correlation tests between intrinsic RGB width and various parameters including metallicity, age and mass-based parameters. Then we derive the normalized RGB width by removing the effect of metallicity on intrinsic RGB width and repeat the correlation tests followed by comparing Galactic and MC GCs in the mass-RGB width plane.

In chapter 5, we discuss our results in association with other studies. We consider previous studies that explored the role of age and host galaxy and discuss them in the context of this thesis.

In chapter 6, we present the summary of our results and discuss future prospects.

There are two appendices attached. Appendix A consists of figures that offer additional information about the content of chapter 4. Appendix B consists of figures that deal with discussions in chapter 5.

Chapter 2

Observations and Data Reduction

2.1 Observations

We retrieved observations of NGC 1898 and NGC 1786 from the HST MAST Archive collected with WFC3/UVIS in the F336W, F438W and F814W bands. We have also used the observations of NGC 121 in the same aformentioned WFC3/UVIS filters and Lindsay 1 observed with ACS/WFC (Wide Field Camera) in the F555W (V band) and F814W filters and WFC3/UVIS in the F336W, F438W and F343N filters, as used by Lagioia et al. (2019a). We performed photometry on NGC 121 and Lindsay 1 observations to aid in the comparison of our RGB width values considering that there are a few differences (photometry pipeline, PSF computation, quality cuts for selection of stars etc.) between our method and that of Lagioia et al. (2019a). A brief summary of the observations is provided in Table 2.1.

2.2 Data Reduction using DOLPHOT

We use DOLPHOT 2.0 to preprocess the *flt* images and run PSF photometry. *flt* images are debiased and flat-field corrected multi-extension Flexible Image Transport System (FITS) images. DOLPHOT provides pre-computed PSFs for every filter of all cameras onboard HST, pixel area maps (PAMs) and also ready-made modules specific for each camera. It also enables us to perform

Table 2.1: Observation Data Set

Cluster	Date	Camera	Filter	No. x Exposure time (s)	Proposal
NGC 1898	2014 Jan 10	WFC3/UVIS	F336W	2×1035	13435
			F438W	2×200	
			F814W	100	
NGC 1786	2014 Jun 13	WFC3/UVIS	F336W	2×1015	13435
			F438W	2×200	
			F814W	100	
NGC 121	2014 May 16, 2014 Oct 16	WFC3/UVIS	F336W	4×1061	13435
			F438W	4×200	
			F814W	2×100	
Lindsay 1	2003 Jul 11, 2005 Aug 21	ACS/WFC	F555W	$2 \times 20 + 480 + 4 \times 496$	9891, 10396
			F814W	$2 \times 10 + 290 + 4 \times 474$	
	2014 June 19	WFC3/UVIS	F336W	$500 + 4 \times 1200$	14069
			F438W	$500 + 800 + 1650 + 1850$	
			F343N	$120 + 2 \times 460$	

photometry on images obtained from different instruments simultaneously which was useful in the analysis of Lindsay 1 (see Section 2.6). From here on, we summarize the steps involved in preprocessing and PSF photometry of WFC3/UVIS images performed using DOLPHOT. The preprocessing of ACS/WFC images are similar but with different task names. As such, the images from each camera must be preprocessed separately.

UVIS images are 6-extension files with 3 extensions (science image, error array and data quality array) for each (UVIS 1 and UVIS 2) chip. *wf3mask* is used to mask the pixels flagged as bad in the data quality extension of the FITS file and multiply by the PAM to render the images in the units of electrons. PAM corrects for the geometric distortion in *flt* images and matches their output count to those of drizzled images. 'Drizzle' or formally 'Variable-Pixel Linear Construction' is a commonly used method to eliminate the effect of geometric distortion in images (Fruchter & Hook 2002). Then *splitgroups* task is used to convert the images into single-extension FITS files by splitting the images into UVIS 1 and UVIS 2 chips. This is necessary since we use a drizzled image as our reference image. This is followed by employing *calcsky* for obtaining sky images. Then we initiate the DOLPHOT routine for PSF photometry. In the parameter file for the routine, we include the split single extension FITS images and the drizzled reference image. The combination of images in the deepest band, F814W in this case, is usually used as the reference image. But there is only 1×100 seconds of

exposure (see Table 2.1) in that filter for both NGC 1898 and NGC 1786. So, we have consistently used the F438W drizzled image (2 × 200s) as the standard drizzled image. Image alignment is done by using the World Coordinate System (WCS; *UseWCS=1*) and the Charge Transfer Efficiency (CTE) correction for the images is done by setting *WFC3useCTE=1*. CTE is a measure of how well the charges are transferred during image readout from the charge-coupled device. Since HST passes through the South Atlantic Anomaly (SAA) periodically, the high radiation levels cause defects in the detector which traps charges during readout and subsequently releases them opposite to the readout causing losses. Especially, fainter sources suffer a higher fractional flux loss (Baggett et al. 2015 and references within). The rest of the parameters are set according to the recommendations in the manual. The instrumental magnitudes are calibrated to the Vega magnitude system.

2.3 Selection of stars

The output was subject to various quality cuts. We selected stars based on object type, selecting those that are classified as good or too faint for PSF determination, leaving out those that are elongated, extended or too sharp. We removed stars based on error flags, selecting only those stars that have been extremely well recovered from the image and those with photometry apertures extending off the chips. This was followed by filtering out the stars that have a magnitude uncertainty greater than 0.1 mag and with sharpness that lies outside the ±0.1 interval. Beyond that, we only select those stars that are detected in all the three filters used in this thesis. Panel (a) of Figures 2.1 and 2.2 shows the stars in the field of view of WFC3/UVIS. Panel (b) of Figures 2.1 and 2.2 and panel (a) of Figures 2.3 and 2.4 show the stars selected through quality cuts.

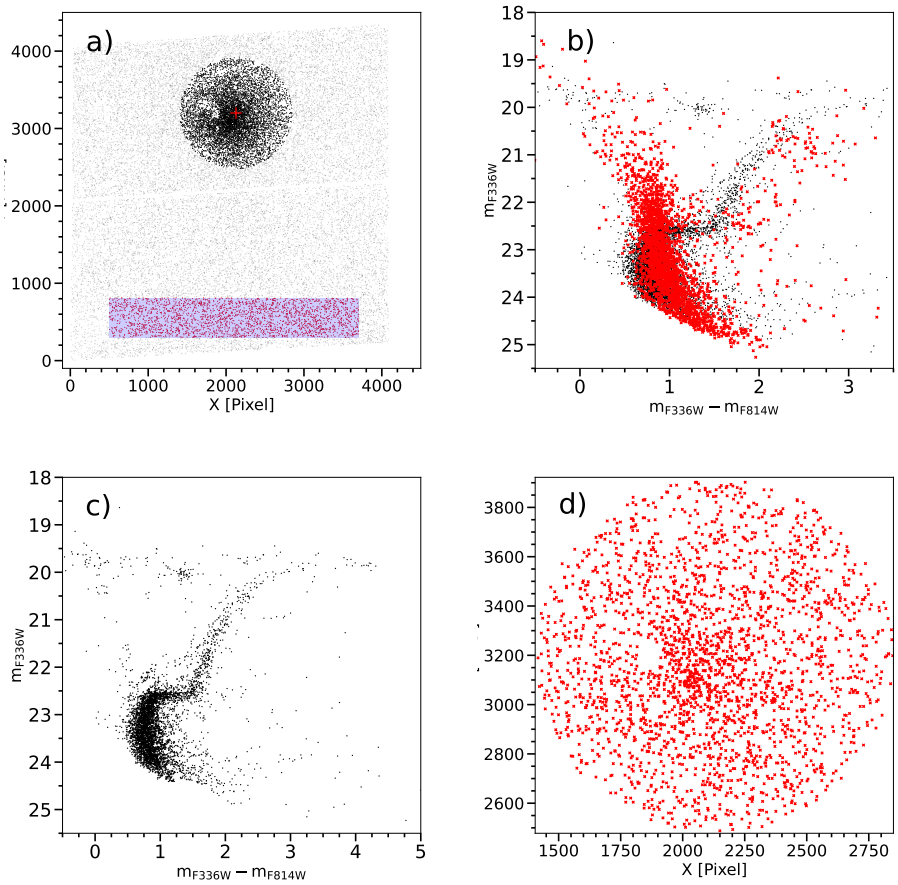

Figure 2.1: Field star removal in NGC 1898 using $m_{F336W} - m_{F814W}$ vs m_{F336W} CMD. *(a):* Coordinate map of the cluster and field stars as observed by UVIS 1 and UVIS 2 chips. Cluster region is highlighted by black dots with the center marked by a red cross. Stars used for statistical subtraction are highlighted with a rectangular box. *(b):* CMD of the cluster core region with field stars marked by red crosses. *(c):* CMD of the cluster core region after the field stars are removed. *(d):* Coordinate map of the eliminated field stars.

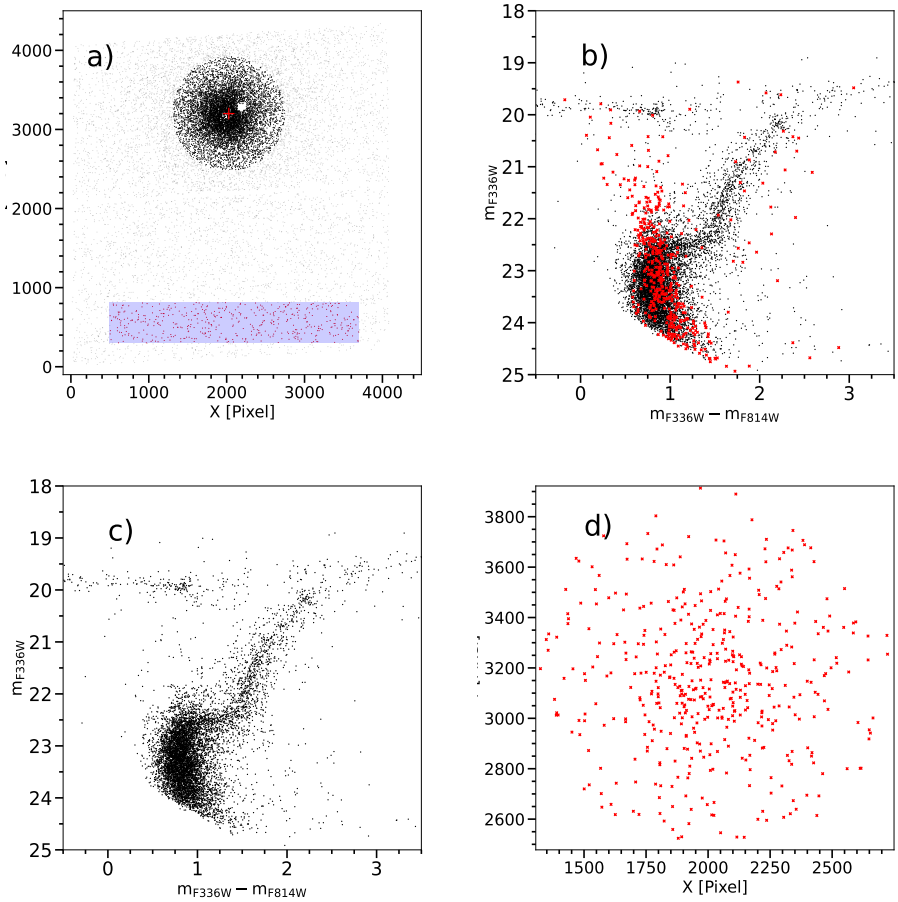

Figure 2.2: Same as Figure 2.1 but for NGC 1786.

This was followed by a statistical removal of field stars. We defined a rectangular reference field region having the same sky area as the circular cluster core region (722 pixel radius for both the clusters) and residing at the edge of the field-of-view, as far away as possible from the cluster area, as seen in panel (a) of Figures 2.1 and 2.2 with the center of the cluster marked with a red cross. The reason for choosing equal areas is that the distribution of field stars is assumed to be homogenous and hence its density will be the same across the image. Since the tidal radii of the clusters are greater than 20 pc (≈20 pc for NGC 1786 and ≈35 pc for NGC 1898, McLaughlin & van der Marel 2005 assuming a King's profile) and the field of view of WFC3/UVIS

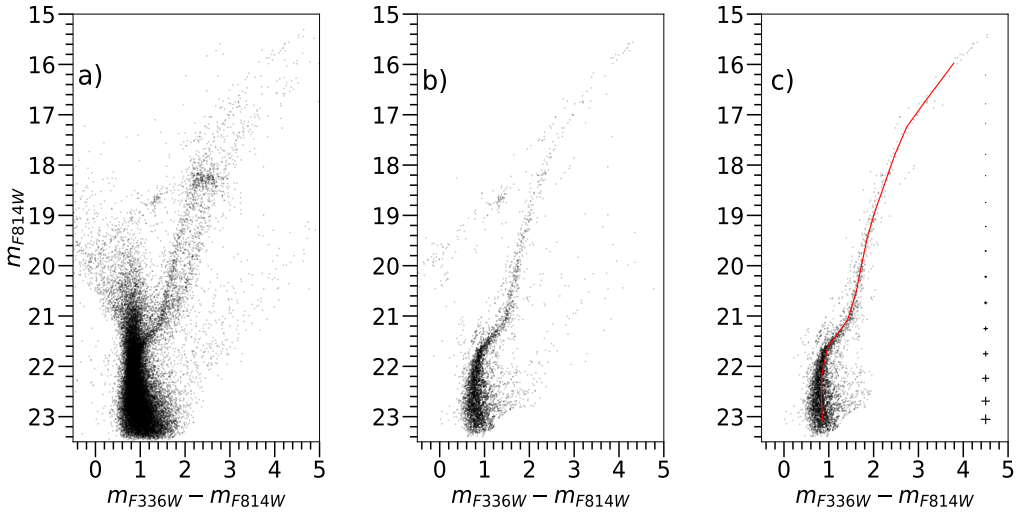

Figure 2.3: $m_{F336W} - m_{F814W}$ vs m_{F814W} CMD of NGC 1898. *(a):* CMD containing stars selected through quality cuts. *(b):* CMD of the cluster core region after field-star subtraction. *(c):* same as (b) after visual selection using TOPCAT with the fiducial line fit along which artificial stars were generated. The photometric error bars are represented on the right side.

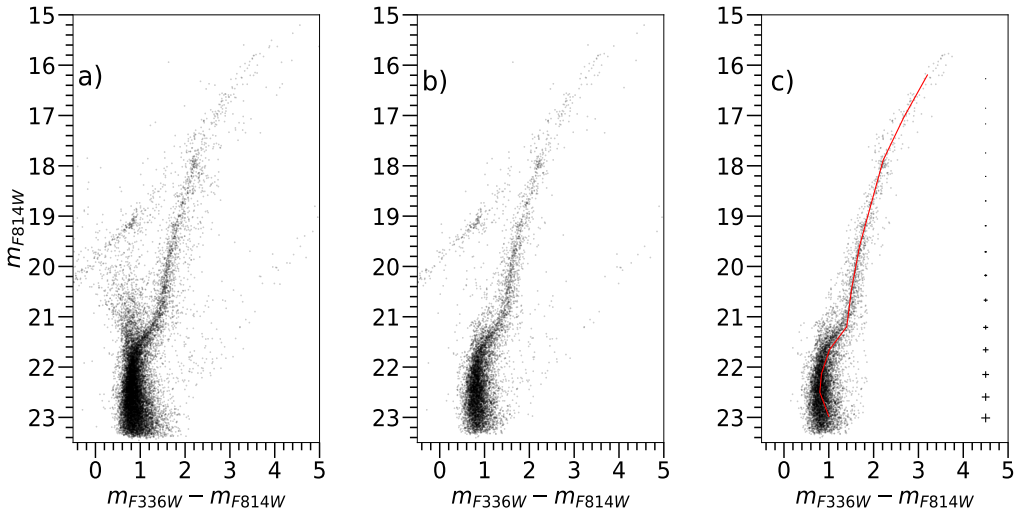

Figure 2.4: Same as Figure 2.3, for NGC 1786.

is ≈38 pc (assuming a distance of 50 kpc to the LMC), a certain fraction of cluster stars in the outer region are inevitably subtracted as field stars. But, as Niederhofer et al. (2015) points out, it is not a serious issue as the oversubtraction mostly affects the well populated regions of the CMD and keeps the overall structure unchanged. We make use of $m_{F336W} - m_{F814W}$ vs m_{F336W} CMD for field star subtraction since we achieved a relatively better separation between cluster stars and field stars in this filter combination. For every star found in the reference field CMD, the star nearest to it in the cluster CMD was eliminated if the difference in magnitude and colour between the two stars was lesser than 0.5 mag and 0.25 mag respectively. Panel (b) of Figures 2.1 and 2.2 show the eliminated field stars marked in red. Panel (c) of Figures 2.1 and 2.2 and panel (b) of Figures 2.3 and 2.4 show the $m_{F336W} - m_{F814W}$ vs m_{F336W} and $m_{F336W} - m_{F814W}$ vs m_{F814W} CMD of the cluster core region after field-star removal respectively. Panel (d) of Figures 2.1 and 2.2 show the coordinate map of the eliminated field stars.

Quality cuts and statistical subtraction of field stars do not get rid of undesirable stars altogether. Certain stars to the red of the RGB branch were recovered in the photometry performed on artificial stars (see section 2.4) in the same regions of the CMD as that of the observed stars but on visual inspection of images, were found to be problematic. Figures 2.5 and 2.6 show some of the outliers in the RGB marked with red dots. Panel (a) in both figures show the location of these stars before the field star subtraction. It could be seen clearly that field stars form a second RGB diverging out of the sub-giant branch. Panel (b) shows that some of the very red stars are retained after the field star subtraction. Panel (c) is the CMD of artificial stars (see Section 2.4) and it could be seen that there are outlying RGB stars at roughly the same colours and magnitudes as in the panel (b) which indicates that they agree with each other. When looked at their position on the images, some of the stars were placed in ring shaped artefacts, some of them were placed in the diffraction spikes of brighter stars (see Figure 2.7) and the rest of the stars, though look apparently distinguished in the image, are considerably off the fiducial sequence of the cluster. So, to be consistent and prevent overestimation, we selected through visual inspection using *TOPCAT* only those stars that lie along and close to the fiducial sequence of the observational CMD (see panel (c) of Figures 2.3 and 2.4). For Lindsay 1, we eliminated a single star since the corresponding region in the synthetic CMD was devoid of stars altogether. So, we assumed it to be a field star.

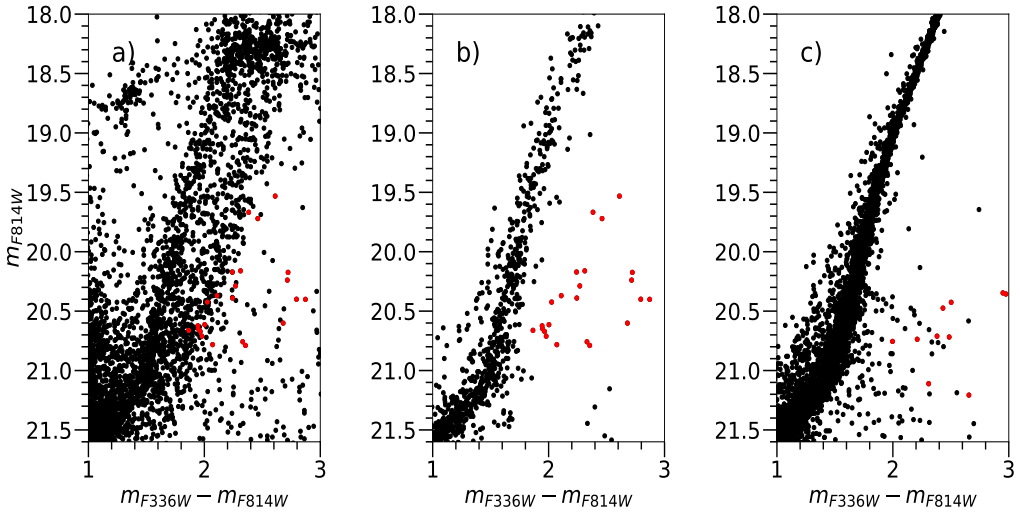

Figure 2.5: $m_{F336W} - m_{F814W}$ vs m_{F814W} CMD of NGC 1898. *(a):* Enlarged section showing the lower RGB before field star subtraction. We can see two strands of RGB diverging from sub-giant branch. Eliminated stars are marked in red. *(b):* RGB branch after field-star subtraction. *(c):* CMD of the artificial stars with the eliminated stars marked in red.

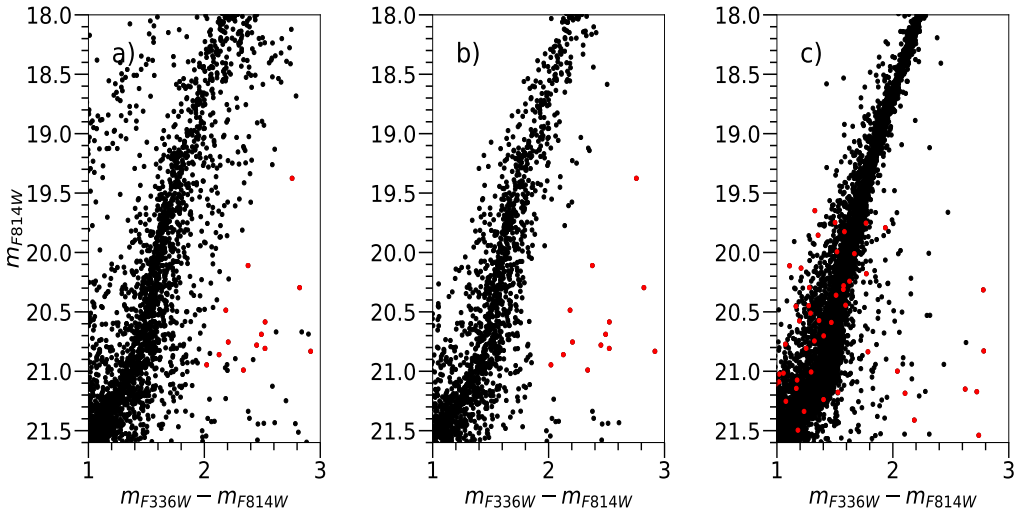

Figure 2.6: Same as Figure 2.5, for NGC 1786.

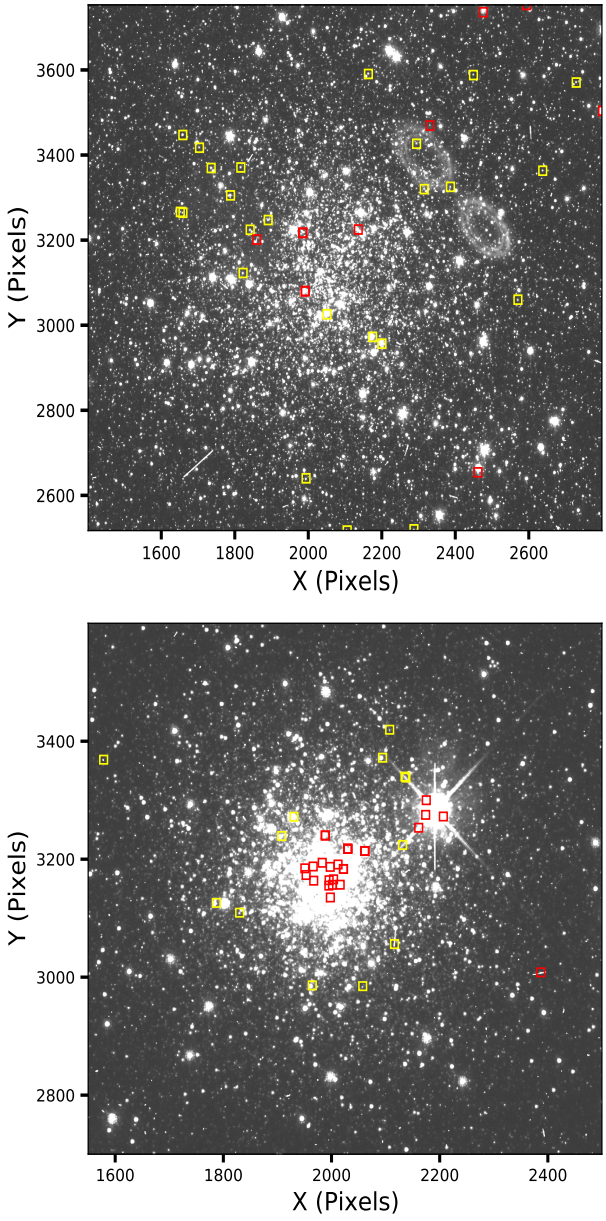

Figure 2.7: Eliminated cluster stars (in yellow) in NGC 1898 (top panel) and NGC 1786 (bottom panel) along with the eliminated artificial stars (in red) are marked.

2.4 Artificial stars

Artificial stars (ASs) were used to produce synthetic (pseudo-)CMDs, compare them with observational CMDs and also estimate the photometric error. We followed the method described in detail in Anderson et al. (2008) and summarized here. We fit a fiducial line on the cluster CMD and generated 50,000 stars with random magnitudes that lie on the fiducial line, with proportionate distribution in each bin. Here, for every random F814W magnitude, we generated a F336W magnitude and F438W magnitude that lie on the fiducial line of $m_{F336W} - m_{F814W}$ vs m_{F814W} and $m_{F438W} - m_{F814W}$ vs m_{F814W} CMD respectively. The coordinates of the stars were generated by defining a circular cluster area and generating coordinates within the circumference of the circle. We introduced an offset of 50 pixels on each axis of the coordinate map relative to the observational CMD. The artificial stars were added to the science images one at a time to prevent crowding. Photometry was performed with the same parameters as for the real images and the same quality cuts were applied as well. The CMD of artificial stars too show outliers as shown in panel (c) of Figures 2.5 and 2.6. Due to the huge number of stars in the artificial catalogue, elimination through visual inspection proved to be difficult. So, we eliminated the stars whose difference in output and input magnitude was greater than 1.5 mag in any of the three filters. Though this doesn't eliminate all of the undesirable stars, it has the advantage of getting rid of a sizeable number of them without eliminating a significant number of well measured stars. Figure 2.7 shows the visually eliminated artificial stars marked as red squares and the eliminated cluster stars as yellow squares in NGC 1898 and NGC 1786.

2.5 Differential Reddening Correction and PSF zero point variation

Differential reddening (DR) refers to the spatially variable extinction resulting from the absorption and scattering of blue light by the interstellar medium and makes the target appear redder than it actually is. Colour variations may also result from shifts in photometric zero points caused by small unmodelable PSF variations. If the colour variations caused by DR and unmodelable PSFs are unaccounted for, it may result in false detection of MPs. We corrected for the effects of differential reddening and PSF zero

point variation following approximately the method described in Milone et al. (2012a). The procedure is described here. The optical CMD m_{F438W} − m_{F814W} vs m_{F814W} was used for this purpose and the procedure is demonstrated in Figure 2.8 using NGC 1786. A new reference frame is adopted in which the origin of the CMD was shifted arbitrarily to a point near the main sequence turn-off (MSTO) magnitude and then the CMD was rotated counterclockwise through an angle θ defined by:

$$\theta = arctan \frac{A_{\mathrm{F438W}} - A_{\mathrm{F814W}}}{A_{\mathrm{F814W}}}$$

where A_x denotes the extinction in filter x. The new reference frame is easier to work with since the horizontal axis represents the direction of the reddening vector rather than the oblique reddening line in the non-translated CMD. The horizontal axis of the new reference frame shall henceforth be called 'Colour' and the vertical axis 'Magnitude'. We selected the MS stars between 0.55 and 0.2 mag along the 'Magnitude' axis as reference stars, divided them into 6 bins and fit a quadratic spline to the median 'Colour' points determined with a 3-sigma clip in each bin. Panels (a) and (b) of Figure 2.8 show the $m_{F438W}-m_{F814W}$ CMD and the MS reference stars in the translated CMD respectively. The reference stars are marked as blue dots in panel (a) and the fiducial line of the MS reference stars is represented by a continuous red curve in panel (b). For each reference star (target), the distance from the fiducial line (Δ'Colour') is determined, then substituted with the median Δ'Colour' of the 70 nearest reference stars excluding the target star as demonstrated in the panels (c) and (d) of Figure 2.8. Then we divided the pixel coordinate map of the cluster into 15 × 15 grid with each cell consisting of 97 × 97 pixels. This is followed by determining the median Δ'Colour' of the reference stars in each cell of the 15 × 15 grid and then smoothing using 2D tophat filter. Panel (e) consists of two sub-panels. The top panel shows a cell in the 15 × 15 grid that lies in the core of the cluster and the bottom shows one that lies towards the outskirts of the cluster. The reference stars are marked as red dots in both panels. Panel (f) shows the Δ'Colour' histogram in these two cells with the red and black lines representing the median of the reference stars before and after tophat convolution respectively. The smoothed median Δ'Colour' of each cell in the 15 × 15 grid is subtracted from 'Colour' of each star in the cell. A fiducial line was then fit to the reference stars in the translated CMD and it was near identical to the one fit to the non-corrected reference stars at the start of

this procedure, as demonstrated in panel (g) of Figure 2.8. It indicates the goodness of the fit. The smoothed median Δ'Colour' of the cells in the grid are then converted to E(B−V) and then to filter specific extinction using the following relation for total-to-differential absorption obtained from Aaron Dotter (Dotter 2016) by Lagioia et al. (2019a):

$$E(B-V) = \frac{A_{\mathrm{F336W}}}{5.100} = \frac{A_{\mathrm{F438W}}}{4.182} = \frac{A_{\mathrm{F814W}}}{1.842}$$

It is then followed by subtracting the extinction magnitudes from the observed magnitudes in the respective filters. The corrected $m_{F438W} - m_{F814W}$ vs m_{F814W} is shown in panel (h) of Figure 2.8. DR map of NGC 1786 is shown in Figure 2.9.

The average E(B−V) of NGC 1898 is less than 0.10 mag (McLaughlin & van der Marel 2005). Since the variation of the reddening across the cluster field has such a negligible effect on the CMD, we applied corrections only to photometric zero point variations due to slight unmodelable PSF variations. The procedure for correction is almost the same as the correction for DR but along the direction of pseudo-colour $C_{F336W,F438W,F814W}$ instead of the direction of reddening vector and without shifting the origin of the CMD. Figure 2.10 depicts the results of DR correction and PSF zero point correction of NGC 1786 and NGC 1898 using $m_{F336W} - m_{F814W}$ *vs* m_{F814W} CMD and $C_{F336W,F438W,F814W}$ vs m_{F814W} pseudo-CMD respectively. The pseudo-colour variation due to zero point shift in NGC 1898 is 0.001 mag.

2.6 NGC 121 and Lindsay 1

Since we wanted to quantify the possible offsets between our results and those of Lagioia et al. (2019a) due to differences in our method, we attempted to reproduce their results using our techniques. We selected two SMC clusters for analysis: NGC 121 and Lindsay 1. For these two clusters, Lagioia et al. (2019a) performed photometry on images taken with F555W and F814W filters from ACS/WFC and F343N filter from WFC3/UVIS apart from those taken with the three WFC3/UVIS filters used in this thesis. We performed photometry on the exact dataset of Lindsay 1 as used in Lagioia et al. (2019a) but restricted ourselves to the three standard filters for NGC 121 without considering even the images taken with ACS/WFC F814W filter. In the case

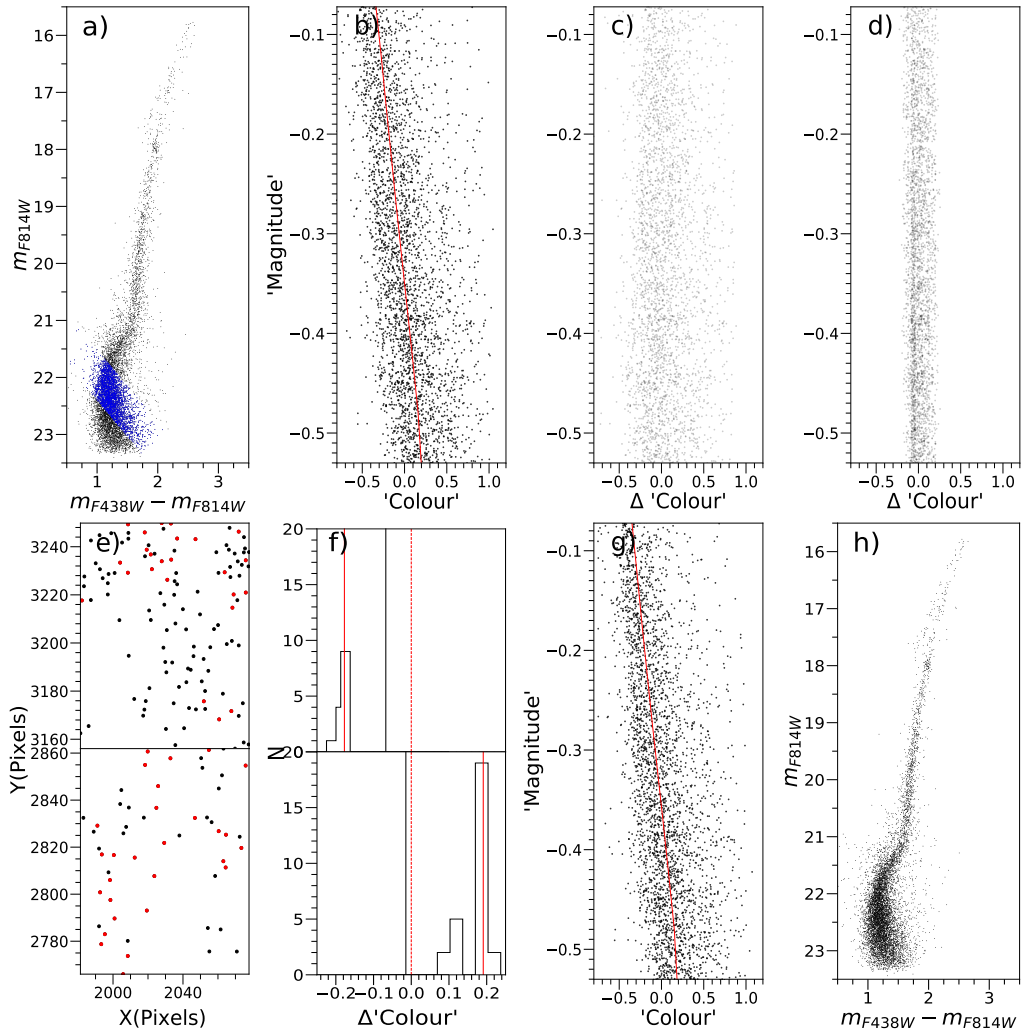

Figure 2.8: Method for correcting DR illustrated using NGC 1786. *(a):* $m_{F438W} - m_{F814W}$ vs m_{F814W} CMD. The blue dots represent the selected reference stars in the translated CMD. *(b):* The translated CMD with the reddening direction parallel to the x-axis. The red curve represents the fiducial line fit of the reference stars. *(c):* The translated CMD after the subtraction of the 'Colour' of fiducial line from the 'Colour' of each star at the same magnitude. *(d):* The Δ'Colour' of each star in *(c)* is replaced by Δ'Colour' of its 70 nearest neighbours in the pixel-coordinate map. *(e):* Two bins, one in the core of the cluster and the other in the outskirts, in the 15×15 grid division of the pixel coordinate map are shown. The red dots indicate the reference stars in the bins. *(f):* Histogram of the Δ'Colour' distributions in the two bins shown in *(e)*. The continuous red line and black line indicate the median 'Colour' of the reference stars before and after tophat convolution respectively. *(g):* The translated CMD after the subtraction of tophat smoothed median Δ'Colour' of the reference stars from the 'Colour' of stars in all the cells of the 15×15 grid. The red line indicates the fiducial line of the new CMD. *(h):* The CMD after it is rotated back to the original reference frame.

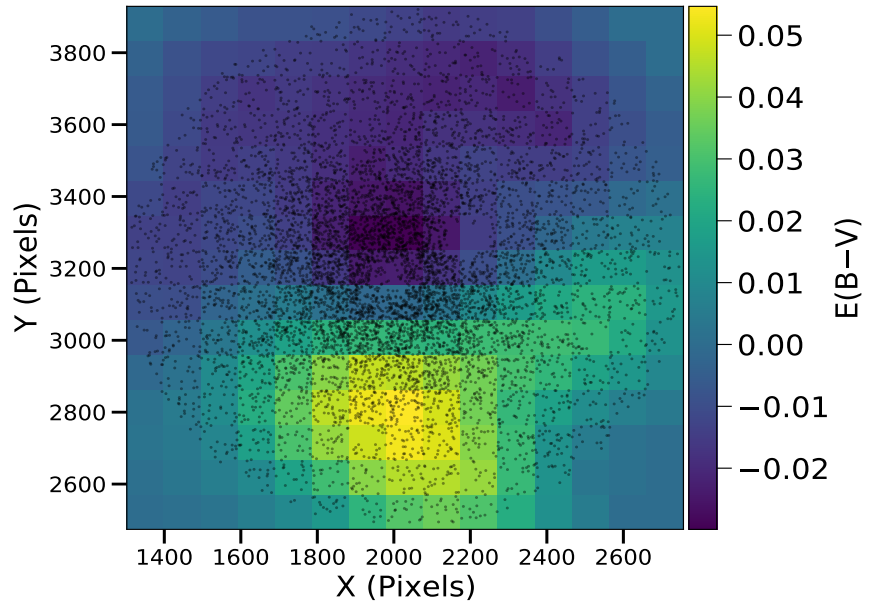

Figure 2.9: Differential Reddening map of NGC 1786.

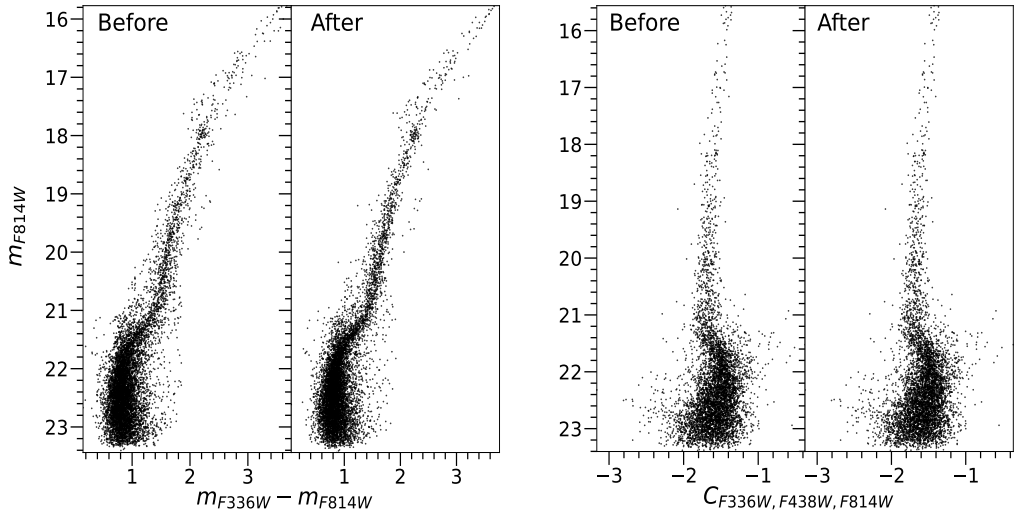

Figure 2.10: Left panel shows $m_{F336W} - m_{F814W}$ vs m_{F814W} CMD of NGC 1786 before and after DR correction. Right panel shows $C_{F336W,F438W,F814W}$ vs m_{F814W} pseudo-CMD of NGC 1898 before and after PSF zero point correction.

of Lindsay 1, the selection criteria for stars after photometry didn't include the presence (or lack thereof) of magnitudes of stars in the ACS/WFC F555W filter and WFC3/UVIS F343N filter. The only difference lies in the inclusion (or lack thereof) of ACS/WFC F814W images in the NGC 121 photometry. This approach helps us to decide the importance of including ACS/WFC F814W images in future studies depending on whether we are able to obtain a consistent intrinsic RGB width as Lagioia et al. (2019a).

2.7 Cluster Parameters

For Galactic GCs, we obtained current cluster mass (M_c) from Baumgardt & Hilker (2018), initial cluster mass (M_{ini}) from Baumgardt et al. (2019, private communication), metallicities ([Fe/H]) from Harris (1996, 2010 version) and ages from Dotter et al. (2010, 2011), VandenBerg et al. (2013) and Milone et al. (2014). For SMC clusters (Lindsay 1, Lindsay 38, Lindsay 113, NGC 121, NGC 339 and NGC 416) and LMC cluster NGC 1978, M_{ini} was obtained from Milone et al. (2020), total cluster masses were obtained from Glatt et al. (2011) and Chantereau et al. (2019), ages from Lagioia et al. (2019b), Glatt et al. (2008) and Milone et al. (2009).

For NGC 1898 and NGC 1786, the parameter values and their sources are listed in Table 3.1. We derived their initial masses using the methods and programs presented in Goudfrooij et al. (2011, 2014). It involved considering the evolution of cluster mass of model clusters without significant initial mass segregation because both the clusters are classical. The primary effects considered in the estimation of the long term mass loss, estimated from 100 Myr onwards, were stellar evolution and internal mass-density dependent evaporation. Time-dependent mass loss was evaluated using masses at the mean age of the clusters. The initial masses and current masses of Galactic GCs used in this thesis derived by Baumgardt et al. (2019) are updated versions based on *Gaia* Early Data Release 3 (EDR3, Gaia Collaboration et al. 2021). Although the initial masses of Galactic and MC GCs used in this thesis are up to date, there are a lot of uncertainties associated with their determination due to the insufficient knowledge of the evolution of these galaxies and their tidal fields, mass loss and initial mass segregation in these clusters (see Section 2.2 in Milone et al. 2020).

Chapter 3

Measurement of intrinsic RGB width

In this section, we describe the method to deduce the intrinsic RGB width of the clusters in the pseudo-colour $C_{F336W,F438W,F814W}$, as outlined in Lagioia et al. (2019a).

3.1 Derivation of observed RGB width

Panel (a) of Figures 3.1 and 3.2 represents $C_{F336W,F438W,F814W}$ vs m_{F814W} CMD with the stars represented by black dots and photometric error bars on the panel's right side. We started with measuring the MSTO point. This is done by using the naive estimator as explained in Silverman (1986) and is summarized here. We divided the magnitude range (minimum mag to maximum mag in F814W filter) into 15 bins and found the median pseudo-colour and median magnitude in each bin. We repeated the procedure for different bin series by changing the initial point of the first bin by a quantity equal to a fraction of the predefined bin width. This was followed by box car averaging three adjacent points of the resulting median magnitudes and pseudo-colours, the purpose of which is to smoothen the curve connecting the points. The magnitude corresponding to the bluest pseudo-colour in the linear interpolation function of the boxcar averaged points was taken to be the MSTO magnitude (m_{MSTO}). m_{MSTO} is 22.100 mag for NGC 1898 and 22.166 mag for NGC 1786, in F814W filter. We then defined a luminosity interval of 1 mag centered at the reference F814W magnitude which is defined as 2 mag brighter than m_{MSTO} ($m_{MSTO} - 2$).

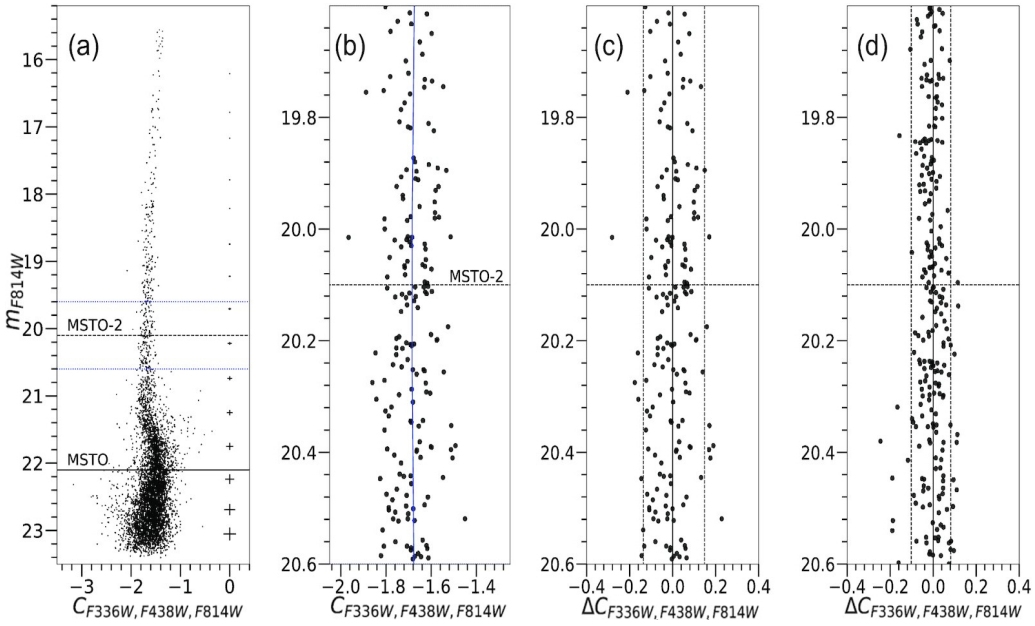

Figure 3.1: Method to determine the intrinsic RGB width of NGC 1898. *(a):* $C_{F336W,F438W,F814W}$ vs m_{F814W} pseudo-CMD. The solid back line represents m_{MSTO} while the broken black line represents $m_{MSTO} - 2$ mag. The broken blue lines represent the selected magnitude interval. The photometric error bars are represented on the right side. *(b):* Fiducial line fit for the selected 1 mag interval. *(c):* Verticalized CMD in the 1 mag interval. The broken black lines represent the 4th and 96th percentile of distribution of pseudo-colour difference, representing W_{obs}. *(d):* Width due to photometric uncertainties as reconstructed from AS test.

Then we calculated the fiducial line of RGB stars as described by the procedure above and got the pseudo-colour difference by subtracting the colour of each star from the fiducial line at the same m_{F814W}. We used moving average for NGC 121 and Lindsay 1 instead of box-car average to estimate the fiducial line since it gave us a better fit. Pseudo-colour difference in the RGB interval gives us the spread resulting from abundance variations (including photometric errors) and verticalizes the CMD. Panel (b) of Figures 3.1 and 3.2 shows the fiducial line of the RGB interval of NGC 1898 and NGC 1786 respectively, represented by a blue curve. The difference betweeen the 4th percentile and 96th percentile of the distribution of pseudo-colour difference was taken as the observed RGB width (W_{obs}), as demonstrated in panel (c) of Figures 3.1 and 3.2. The obtained W_{obs} of

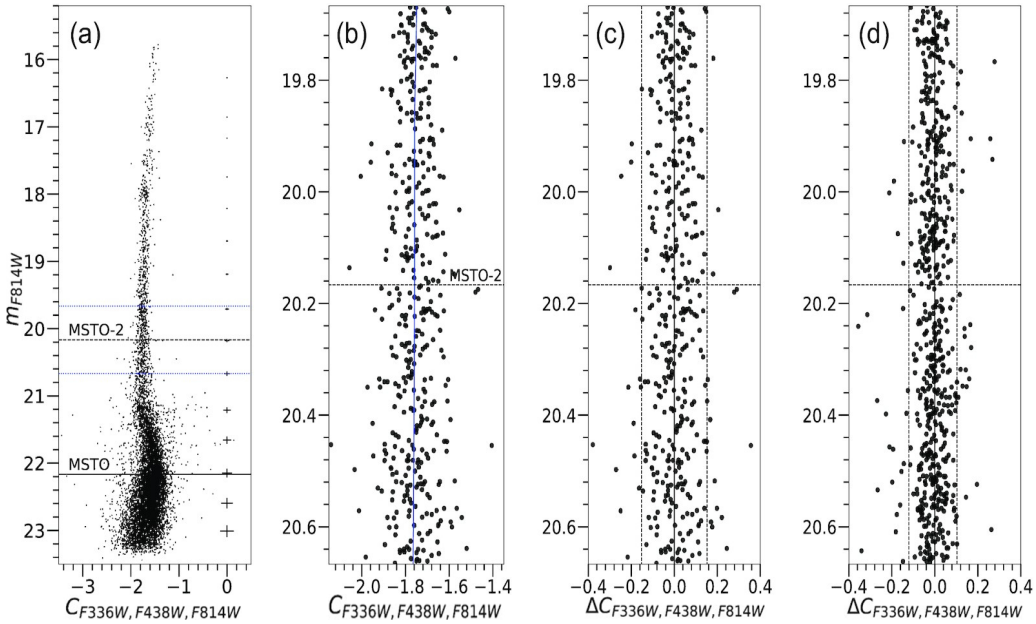

Figure 3.2: Same as Figure 3.1, for NGC 1786

NGC 1898 was 0.284 mag and that of NGC 1786 was 0.304 mag.

The error associated with the observed width was determined by a bootstrapping test. This involves generating random copies of the observed stellar pseudo-colours in the selected RGB interval with replacement. First, we generated 1000 copies of the observed pseudo-colours in the selected interval. It was followed by a random extraction of subsample containing pseudo-colours equal to the number of stars in the selected interval and then we calculated the RGB width for this extraction. We repeated this test 10,000 times. The difference between the observed width and the 68.27$^{\text{th}}$ percentile of the 10,000 bootstrapping measurements of the RGB width was considered as the standard error of the observed width. The associated error obtained was 0.011 mag for NGC 1898 and 0.018 mag for NGC 1786.

3.2 Accounting for photometric errors

The observed RGB width of a cluster is not its intrinsic RGB width since it is not accounted for the contribution by photometric errors. To filter this unwanted contribution and obtain the intrinsic RGB width of the cluster, we estimated the photometric error using ASs. The procedure to calculate

is explained hereafter. We started with a random selection of a subsample from the AS catalogue equal to the number of observed stars in the analyzed magnitude interval. The pseudo-colour difference was calculated by finding the difference between the input and output magnitude of each AS in the subsample. The RGB width of the AS subsample is the difference between the 4th percentile and 96th percentile of the subsample. It represents the contribution of photometric error to W_{obs}. This value was then subtracted in quadrature from the observed RGB width. We repeated this procedure 10,000 times and the average of those 10,000 measurements was taken as the intrinsic RGB width ($W_{CF336W,F438W,F814W}$). Panel (d) of Figures 3.1 and 3.2 represents the error width obtained during one of the runs. The associated error of the RGB width from ASs was obtained by the bootstrapping method described in Section 3.1 and it was then added in quadrature with the associated error of W_{obs}. The resulting error was adopted as the total uncertainty of $W_{CF336W,F438W,F814W}$. The obtained intrinsic RGB widths of NGC 1898 and NGC 1786 were 0.199 mag and 0.185 mag respectively with a total uncertainty of 0.014 mag and 0.019 mag respectively.

We applied the above procedure for the rest of the clusters analyzed in this thesis. The results are tabulated in Table 3.1. For NGC 121 and Lindsay 1, the determined intrinsic RGB width is in line with the results of Lagioia et al. (2019a) within the estimated uncertainties. Lagioia et al. (2019a) determined the intrinsic RGB widths of NGC 121 and Lindsay 1 to be 0.157±0.008 and 0.135±0.009 respectively while our results are 0.169±0.015 and 0.142±0.011 respectively. Considering that ACS/WFC F814W data was not used for NGC 121, this agreement in the values of intrinsic RGB width indicates that F814W magnitude values obtained from both cameras (WFC3 and ACS) are inherently very similar to each other, in line with the synthetic photometry results of Deustua & Mack (2018).

Table 3.1: Metallicity, current mass, initial mass, intrinsic and normalized RGB width values of the analyzed globular clusters

ID	[Fe/H] (dex)	References	M_c ($M_\odot$)	References	M_{ini} ($M_\odot$)	References	$W_{CF336W,F438W,F814W}$ (mag)	$\Delta W_{CF336W,F438W,F814W}$ (mag)
NGC 1898	−1.32	2,3,4	2.24×10^5	6	4.50×10^5	9	0.199 ±0.014	0.050
NGC 1786	−1.80	1,2,3	3.72×10^5	6	1.90×10^6	9	0.185 ±0.019	0.068
NGC 121	−1.30	5	3.70×10^5	6	7.08×10^5	8	0.169 ±0.015	0.019
Lindsay 1	−1.14	5	$\sim 2 \times 10^5$	7	3.39×10^5	8	0.142 ±0.011	−0.019

1.Mucciarelli et al. (2009) 2.Beasley et al. (2002) 3.Olszewski et al. (1991) 4.Johnson et al. (2006) 5.Lagioia et al. (2019b) 6.McLaughlin & van der Marel (2005) 7.Glatt et al. (2011) 8.Milone et al. (2020) 9.This thesis

Chapter 4

Effect of mass on RGB width

4.1 Correlation tests between intrinsic RGB width and global parameters

Lagioia et al. (2019a) conducted a Spearman's rank correation test to find out the correlation between $W_{CF336W,F438W,F814W}$ and the global parameters (metallicity, age, mass etc.). The correlation is quantified by Spearman's rank correlation coefficient (R_s) and the significance of the correlation is given by p-value. $R_s = -1$ represents perfect negative correlation while $R_s = 1$ represents perfect positive correlation. p-value represents the probability of finding an R_s value equal to or larger than the actual one. $p < 0.05$ indicates strong evidence for correlation while $p < 0.01$ indicates a highly significant correlation. Lagioia et al. (2019a) found a highly significant correlation between the $W_{CF336W,F438W,F814W}$ and [Fe/H] with R_s being 0.786, indicating a strong monotonicity, with the intrinsic RGB width increasing with metallicity. There was also a highly significant and strong monotonic correlation ($R_s = 0.924$) between $W_{CF336W,F438W,F814W}$ and $W_{CF275W,F336W,F438W}$ (Milone et al. 2017) which shows that both filter combinations are almost equally sensitive to the variation of light elements in MPs. The R_s values of most of the other global parameters (slope of mass function, cluster core radius, age etc.) lie in the interval $\sim \pm 0.5$ (see the top left plot in Figure 4.1) which represents moderate to weak correlation. Figure 4.1 shows the correlation of $W_{CF336W,F438W,F814W}$ with various parameters as determined by Lagioia et al. (2019a).

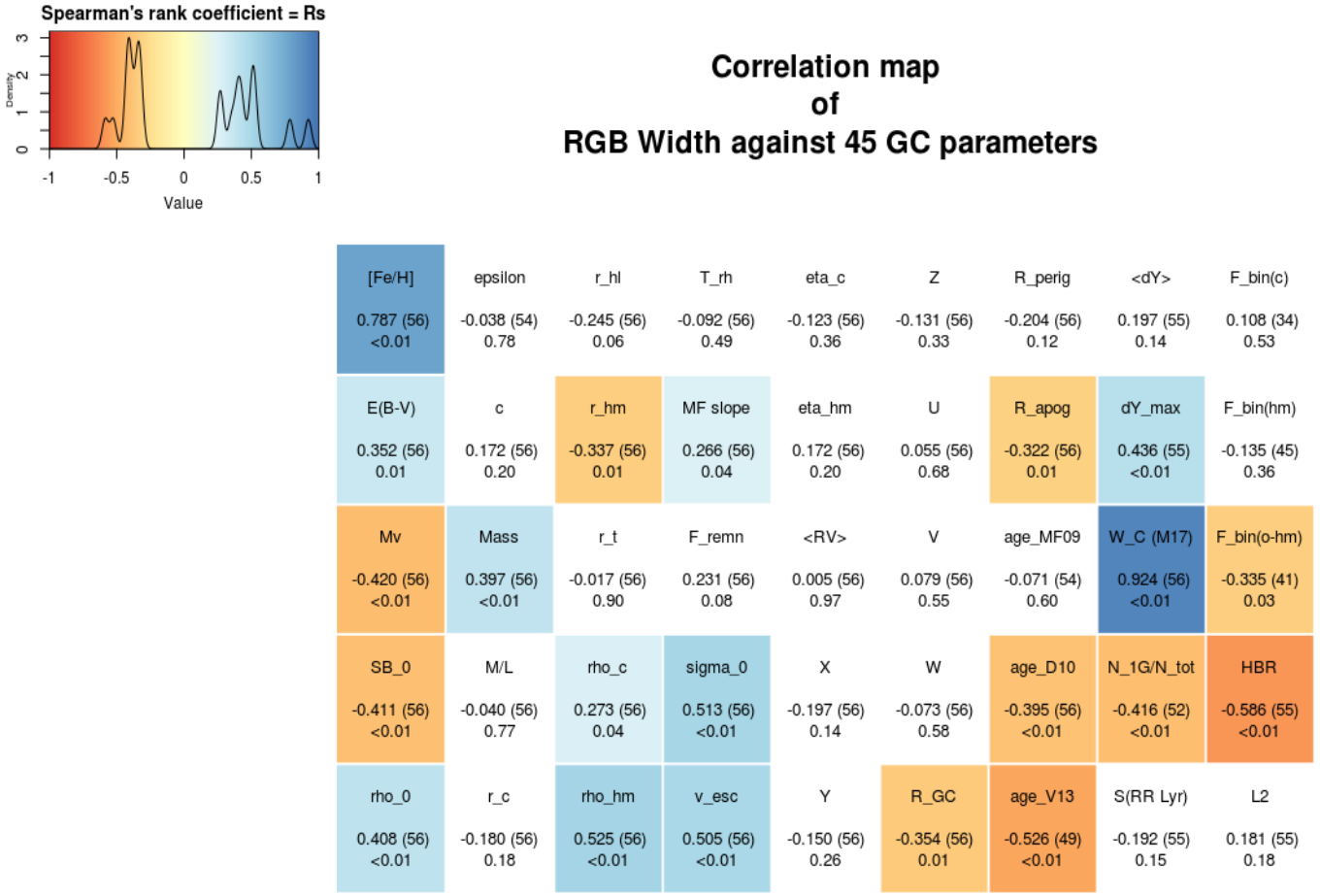

Figure 4.1: Correlation of $W_{CF336W,F438W,F814W}$ with various global parameters. The kernel density distribution of R_s values is shown on the top left. Figure adapted from Lagioia et al. (2019a).

4.2 Correlation tests between normalized RGB width and global parameters

Lagioia et al. (2019a) took into account the effect of metallicity on the rest of the parameters to assess if the correlation with RGB width still holds. The reason for the correlation of RGB width with metallicity is straightforward: there is an increased absorption and scattering of blue light by the metals on the surface of the star which makes it appear redder. So, for a given abundance of C and N, increase in metallicity of the stars increases their spread on the CMD. Lagioia et al. (2019a) subtracted the contribution of metallicity to RGB width using the 58 Galactic GCs used by Milone et al. (2018). Since, massive clusters showed significant scatter in certain metallicity intervals, clusters with $\mathrm{Log}(M_c/M_\odot) < 5.22$ were selected and a linear relation was computed for those clusters since those clusters show adequate linearity. The linear fit, which gives us the relation for RGB width contribution from metallicity, allows us to subtract the effect of metallicity on the RGB width of clusters. This width is called normalized RGB width ($\Delta W_{CF336W,F438W,F814W}$). Spearman's rank correlation test was then carried out to find the correlation of normalized RGB width with the global parameters, as shown in Figure 4.2. It is found that significant and strongly monotonic correlations emerge between intrinsic RGB width and mass and also other parameters such as central velocity dispersion and escape velocity, which are directly linked with mass. This indicates that metallicity and mass have a dominant effect on RGB width and that the observed variance of RGB width cannot be explained by only one of those two quantities. In the $\mathrm{Log}(M_c/M_\odot)$ vs $\Delta W_{CF336W,F438W,F814W}$ plot, it is found that the extragalactic GCs systematically lie beneath the Galactic GCs. There is a significant and monotonic correlation between $\Delta W_{CF336W,F438W,F814W}$ and $\Delta W_{CF275W,F336W,F438W}$, the latter used by Milone et al. (2017), corroborating the earlier observation that both filter combinations are almost equally sensitive.

We used the updated catalogue of current masses and initial masses of Galactic GCs (Baumgardt et al. 2019) based on Gaia EDR3. We performed Spearman's rank correlation test between the intrinsic RGB widths of Galactic GCs obtained by Lagioia et al. (2019a) and [Fe/H], M_c, M_{ini}, mass loss (ML), mass loss per Gyr (MLA), mass loss fraction (MLF) and age. The results of the correlation tests are tabulated in Table 4.1. $W_{CF336W,F438W,F814W}$ scores a strong and significant correlation with [Fe/H], as observed by Lagioia et al.

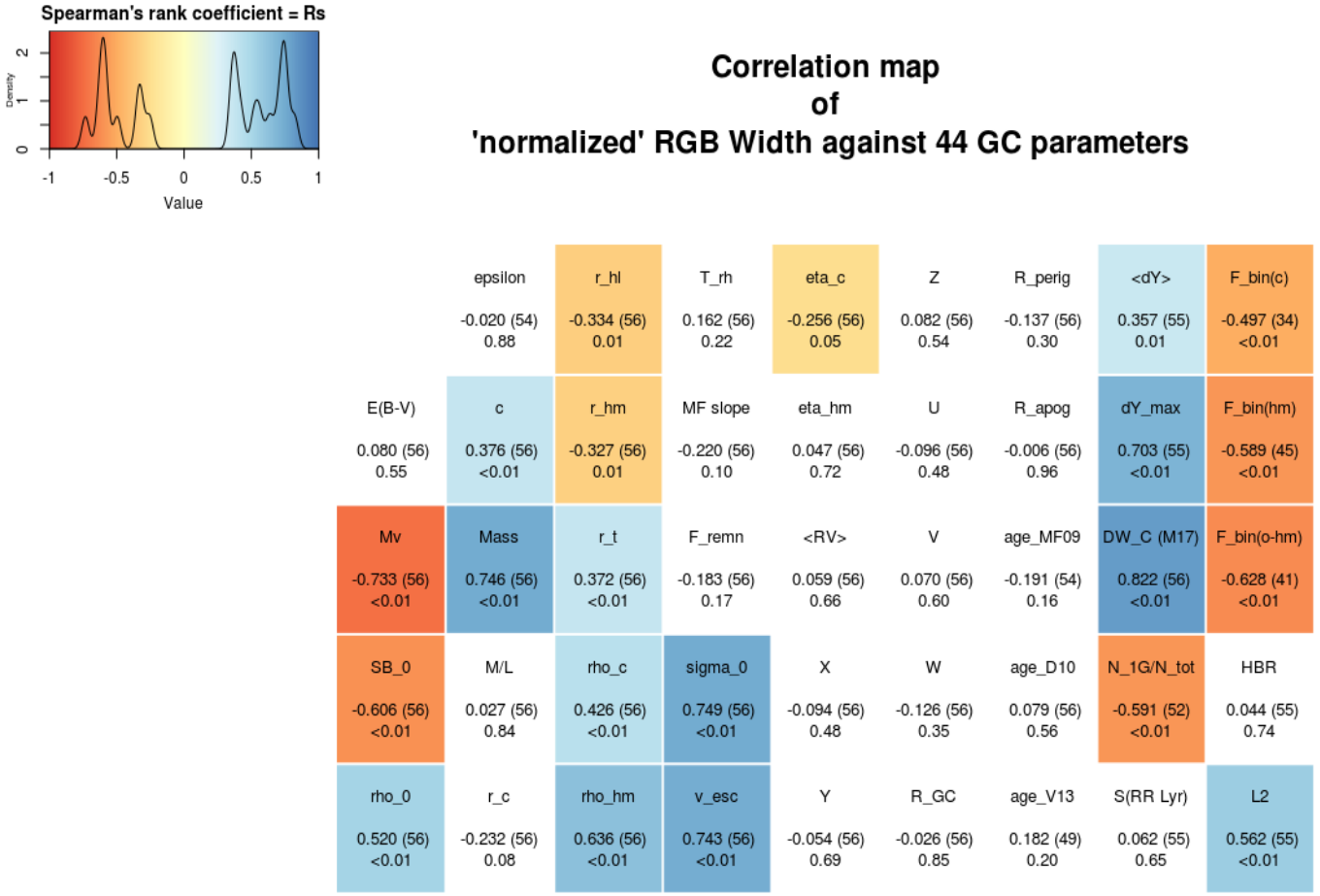

Figure 4.2: Correlation of $\Delta W_{CF336W,F438W,F814W}$ with various global parameters. Figure adapted from Lagioia et al. (2019a).

(2019a). We see that the correlation between $W_{CF336W,F438W,F814W}$ and M_c is no longer significant ($p > 0.01$) with the updated current mass data but we obtained a statistically significant correlation between $W_{CF336W,F438W,F814W}$ and M_{ini} ($p < 0.01$, $R_s = 0.400$). Significant correlations are also observed for MLA and ML. Since the equation of the weighted regression line is dependent on the clusters chosen for the fit and the cluster selection depends on the parameter of choice, we choose to derive two linear relations baseed on the selection of two parameters: M_{ini} and MLF. In the [Fe/H] vs $W_{CF336W,F438W,F814W}$ plot, we selected those Galactic GCs with initial mass less than the median of initial mass distribution of Galactic GCs since they show reasonable linearity, fit a linear relation to those GCs and obtained the metallicity contributed width (W). The same procedure was followed to obtain linear relation by selecting clusters based on MLF. Figure 4.3 shows [Fe/H] vs $W_{CF336W,F438W,F814W}$ plot. The continuous red line represents the regression line while the selected clusters are marked with black filled circles. The regression line represents the width contributed by [Fe/H]. R^2_{adj} is the adjusted determination coefficient and denotes the fraction of the selected clusters accounted for by the regression line. The clusters in the top panel are selected based on M_{ini} while those in the bottom panel are selected based on MLF. The bottom panel shows adequate linearity among the selected clusters though there was no significant correlation between $W_{CF336W,F438W,F814W}$ and MLF. We see that there is marked difference between the two slopes. This is important to consider because W increases with increase in slope and hence, the trends shown by RGB width after the subtraction of the effect of [Fe/H] could differ based on the linear relation used.

We also derived linear relations using ML, MLA and M_c but the regression line derived based on MLF and M_{ini} had the lowest and highest slopes respectively. If there is a marked difference in the trend based on the slope of the regression line, it should be evident by comparing the results of these two scenarios. So, we subtracted W of each cluster from $W_{CF336W,F438W,F814W}$ to obtain the normalized RGB widths- $\Delta W_{CF336W,F438W,F814W,M_{ini}}$ and $\Delta W_{CF336W,F438W,F814W,MLF}$. Figure 4.4 shows the plot of $\mathrm{Log}(M_c/M_\odot)$ vs $\Delta W_{CF336W,F438W,F814W,M_{ini}}$ and $\Delta W_{CF336W,F438W,F814W,MLF}$. Between the two plots, we see that there is a difference in the trend of Galactic GCs whose $\mathrm{Log}(M_c/M_\odot)$ is less than 5. Nevertheless there are no significant differences in the overall trend traced by the GCs and more importantly, no significant differences in the trend traced by the MC GCs with respect to the Galactic GCs which shows that the behaviour of GCs in this space is fairly stable. Since we have determined

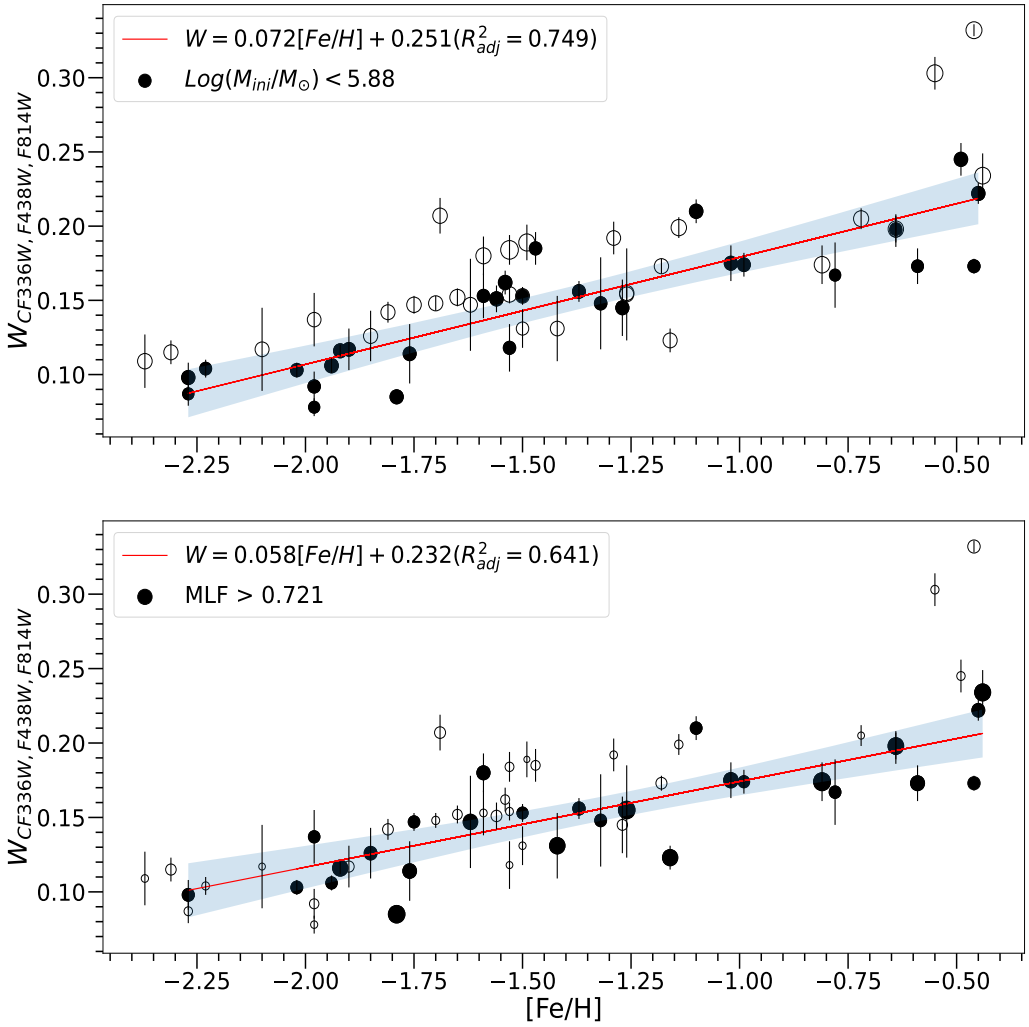

Figure 4.3: [Fe/H] vs $W_{CF336W,F438W,F814W}$ of the 58 Galactic GCs. The shaded GCs are the ones selected for deriving the regression line. The selection criteria for clusters in the top panel is based on M_{ini} while for those in the bottom panel is based on MLF. The size of the clusters is proportional to M_{ini} and MLF in the top and bottom panels respectively. The continuous red line is the regression line. The blue shaded region represents the 95% confidence interval of the regression line. The equation of the line along with the adjusted determination coefficient is indicated in the legend.

that there is no significant difference between the two scenarios, we think the choice of M_c would be more appropriate since the estimates of M_c are relatively much more reliable than M_{ini} and to be consistent with Lagioia et al. (2019a). We followed the same procedure to fit the regression line (see Figure 4.5 for the regression equation), calculated W and subtracted it from intrinsic RGB width to obtain the normalized RGB width (see Table 3.1). We then performed Spearman's correlation test between $\Delta W_{CF336W,F438W,F814W}$ and the aforementioned mass-based parameters. The results are shown in Table 4.1. We see that new correlations emerge after the subtraction of the effect of metallicity. We see that there is a significant correlation between $\Delta W_{CF336W,F438W,F814W}$ and all parameters associated with mass, among which M_c scores the strongest correlation (R_s=0.731), followed by M_{ini}. MLF, which showed no correlation with $W_{CF336W,F438W,F814W}$, shows a significant anticorrelation (R_s= −0.437) with $\Delta W_{CF336W,F438W,F814W}$. The R_s of MLA is almost the same before and after the subtraction of metallicity while that of ML increases marginally.

Table 4.1: Results of Spearman Correlation Test

Parameters	$\mathbf{W_{CF336W,F438W,F814W}}$		$\mathbf{\Delta W_{CF336W,F438W,F814W}}$	
	$\mathbf{R_s}$	**p-value**	$\mathbf{R_s}$	**p-value**
Age	−0.539	< 0.01	0.116	> 0.01
M_c	0.291	> 0.01	0.731	< 0.01
M_{ini}	0.400	< 0.01	0.564	< 0.01
MLF	−0.006	> 0.01	−0.437	< 0.01
MLA	0.429	< 0.01	0.424	< 0.01
ML	0.397	< 0.01	0.444	< 0.01

4.3 Comparison of RGB width against mass

$\mathrm{Log}(M_c/M_\odot)$ and $\mathrm{Log}(M_{ini}/M_\odot)$ vs $\Delta W_{CF336W,F438W,F814W}$ plots are shown in Figure 4.5. Log(MLF), Log(MLA) and Log(ML) vs $\Delta W_{CF336W,F438W,F814W}$ are shown in Figures A.1, A.2 and A.3 respectively. Figure 4.5 shows the two clusters analyzed in this thesis along with the cluster database used in Lagioia et al. (2019a). We find that only two clusters - NGC 339 and NGC 1978 - lie below general trend of the GCs. There is no evidence for the presence of MPs in Lindsay 38 (Milone et al. 2020; Martocchia et al. 2019)

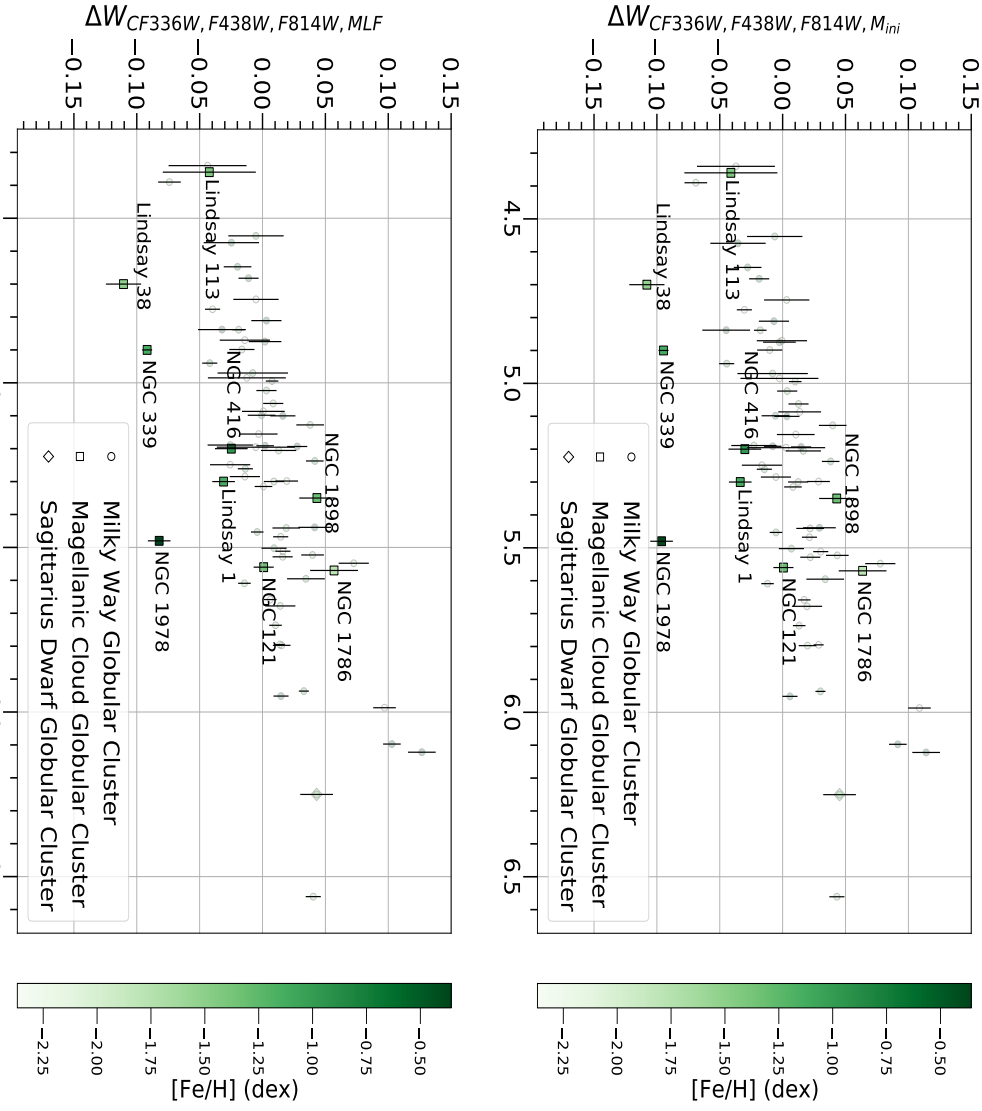

Figure 4.4: Log($M_c/M_\odot$) vs $\Delta W_{CF336W,F438W,F814W,M_{ini}}$ (top panel) and $\Delta W_{CF336W,F438W,F814W,MLF}$ (bottom panel) for the GCs. The colour of the GCs refers to their metallicity while the shape refers to their host galaxy. The vertical lines indicate the uncertainty associated with the RGB width of the clusters. The rest (apart from NGC 1786 and NGC 1898) of the data were obtained from Lagioia et al. (2019a). Also marked are other MC clusters.

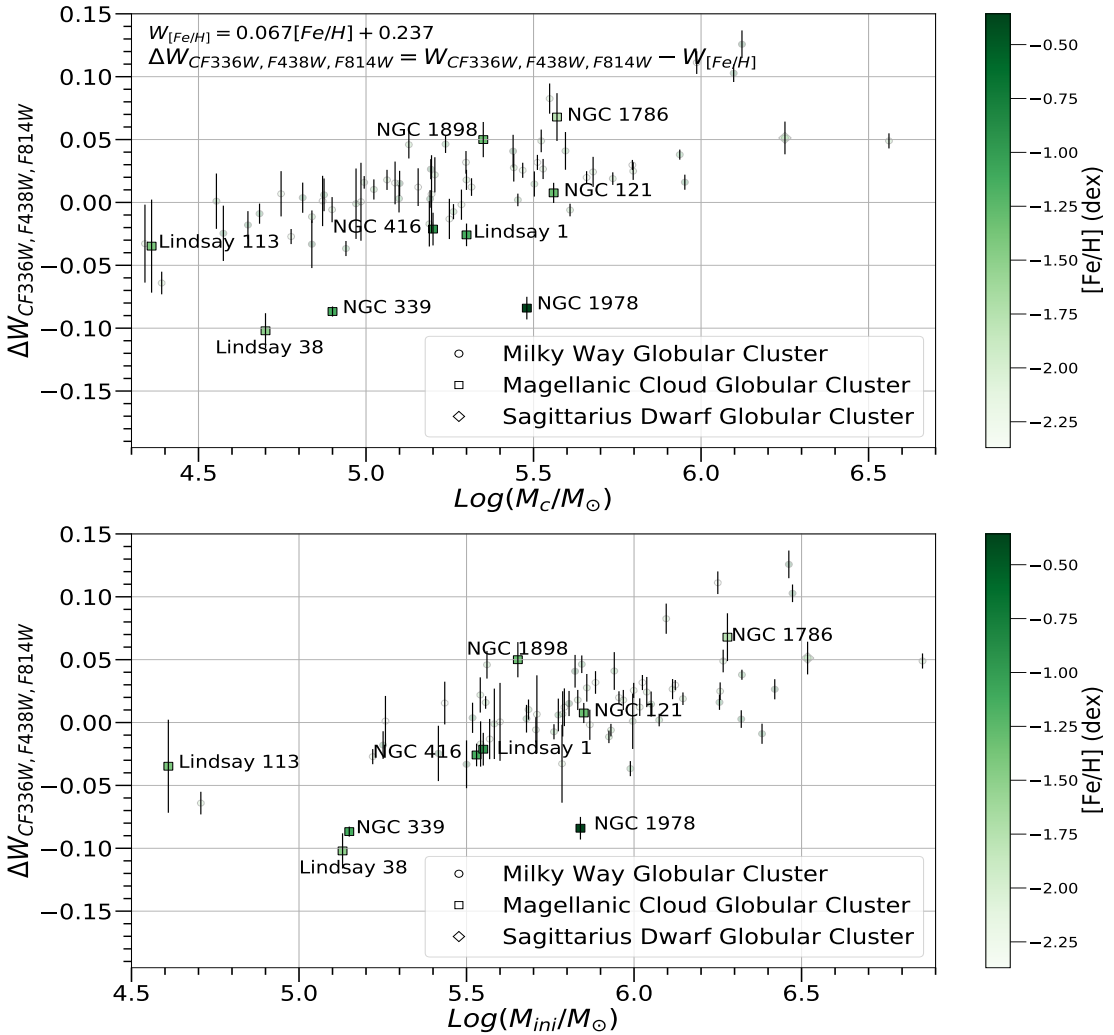

Figure 4.5: Log($M_c/M_\odot$) (top panel) and Log($M_{ini}/M_\odot$) (bottom panel) vs $\Delta W_{CF336W,F438W,F814W}$ for the GCs. The top panel shows the regression equation used to obtain $\Delta W_{CF336W,F438W,F814W}$. We can notice that NGC 1786 and NGC 1898 follow the same trend as the Galactic GCs.

while Lindsay 113 may (Martocchia et al. 2019) or may not (Milone et al. 2020) host MPs. While NGC 416 and Lindsay 1 occupy the lower end, NGC 121, NGC 1786 and NGC 1898 occupy the intermediate and higher ends of the general trend exhibited by the Galactic GCs. That is, five out of seven MC GCs hosting MPs follow the general trend exhibited by the Galactic GCs. Figures A.1, A.2 and A.3 also corroborate this trend. This indicates that galaxy environment may only play a minor role in the formation of MPs in globular clusters.

Chapter 5

Discussion

5.1 Effect of age on MPs

In Figure 4.5, all the three MC clusters occupying the intermediate and higher ends of the general trend exhibited by Galatic GCs are classicial GCs. Whether this indicates a possible role played by age or not remains to be seen. One important drawback is the underwhelming number of observations of MC GCs hosting MPs available in the filter combination used in this thesis. While the correlation tests didn't show any correlation between $\Delta W_{CF336W,F438W,F814W}$ and age, it has to be taken into consideration that Galactic GCs are mostly classical GCs older than 10.5 Gyr. To explore the role of age, we need as many MC GCs across various age ranges as possible.

5.1.1 Evidence suggesting the role of age

There has been a lot of studies exploring the possible effect of age on the manifestation of MPs. Martocchia et al. (2019) analyzed the HST data of four MC GCs in F336W, F438W and F343N filters of WFC3/UVIS complemented with archival data in F555W and F814W filters of ACS/WFC to map the N spread of those clusters. Combined with the data and results of Niederhofer et al. (2017a, b) and Martocchia et al. (2018a, b) totalling 16 MC GCs and 3 Galactic GCs, they found that the standard deviation of observed RGB widths of GCs in $C_{F336W,F438W,F343N}$ and $C_{F343N,F438W,F814W}$ pseudo-colour increase with their age, indicating that cluster age might play an important role alongside metallicity and mass. Figure 5.1 shows age of the GCs plotted against the standard deviation (denoted by σ) of

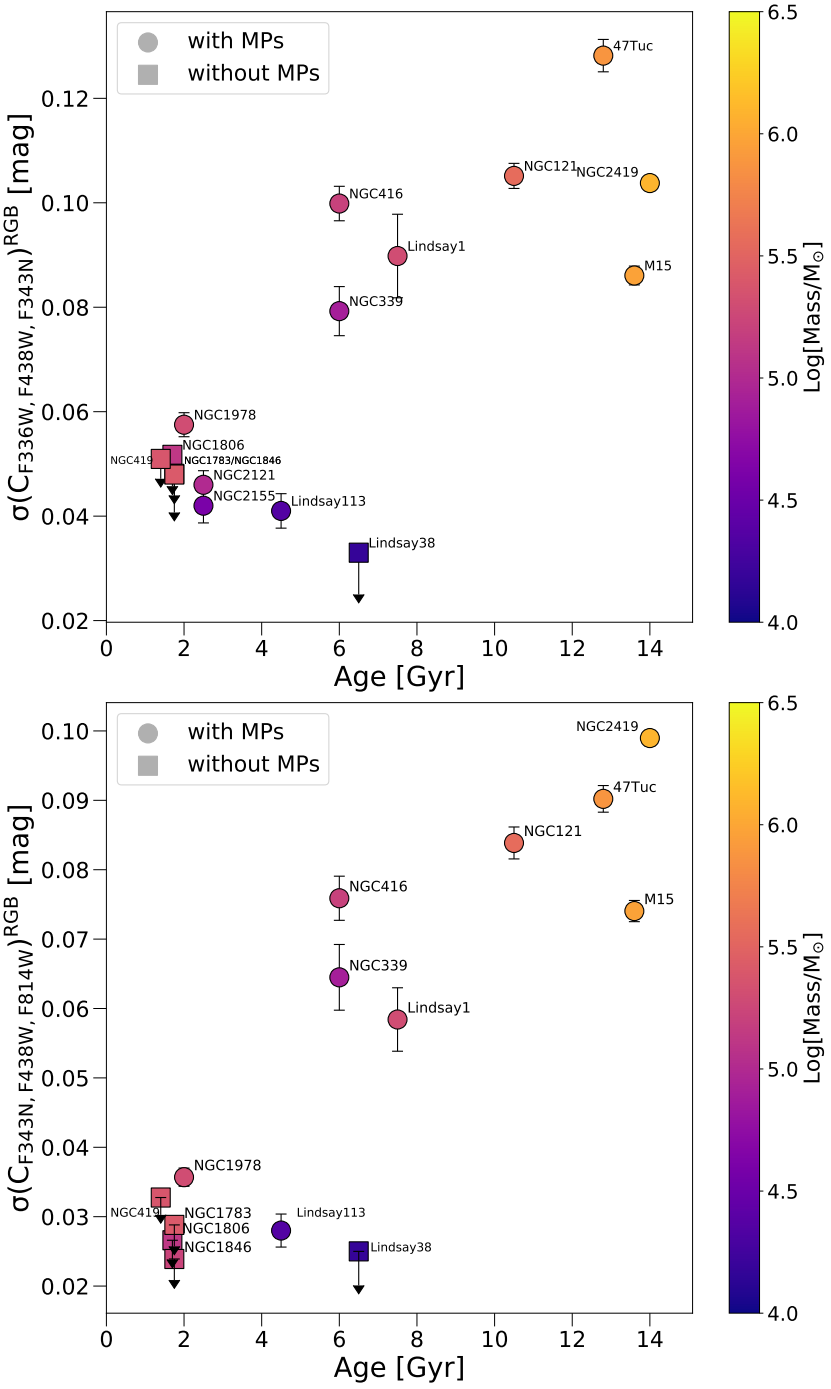

Figure 5.1: Age vs $\sigma(C_{F336W,F438W,F343N})^{RGB}$ (top panel) and Age vs $\sigma(C_{F343N,F438W,F814W})^{RGB}$ (bottom panel) of 16 MC GCs and 3 Galactic GCs (NGC 2419, M15, and 47 Tuc). Figure adapted from Martocchia et al. (2019).

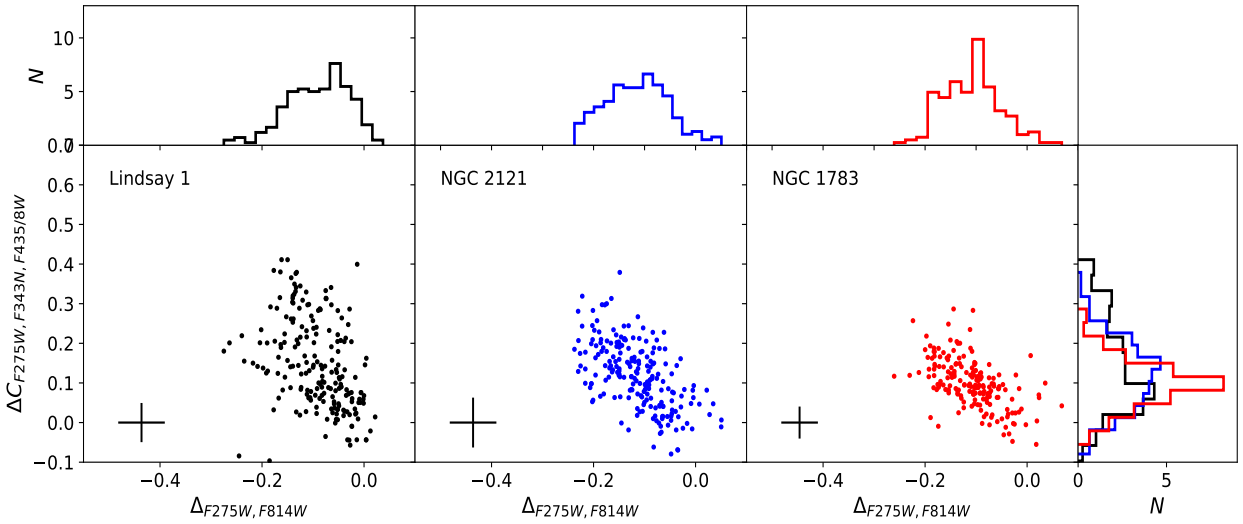

Figure 5.2: $\Delta_{F275W,F814W}$ vs $\Delta C_{F275W,F343W,F435/8W}$ with the histograms of $\Delta_{F275W,F814W}$ distribution on the top and $\Delta C_{F275W,F343W,F435/8W}$ distribution on the right side. We can see that $\Delta C_{F275W,F343W,F435/8W}$ decreases as we go from Lindsay 1 (oldest) to NGC 1783 (youngest). Figure adapted from Saracino et al. (2020).

the RGB widths in the aforementioned filter combinations colour-coded for mass, as determined by Martocchia et al. (2019). They note that Lindsay 38 doesn't host N abundance variations while NGC 416 and NGC 339 do though they have similar ages. But Lindsay 38 has a significantly lower mass than NGC 416 and NGC 339. This indicates that the combined role of age and mass of a cluster may be important for the formation of MPs. Saracino et al. (2020) investigated Lindsay 1 (∼8 Gyr), NGC 2121 (∼2.5 Gyr) and NGC 1783 (∼1.5 Gyr) using the pseudo-colour $C_{F275W,F343N,F435/8W}$[1] and magnitude $m_{F275W,F814W}$ to construct ChMs. Lindsay 1 is an intermediate age cluster and belongs to SMC while the other two are young clusters belonging to LMC. They find that the RGB width in the pseudo-colour $C_{F275W,F343N,F435/8W}$ decreases as the age of the cluster decreases, as shown in Figure 5.2. But they caution that the RGB width can't directly be linked with N abundance variations without accounting for the effects of first dredge-up (Salaris et al. 2020) which makes the determined values of RGB

[1]NGC 1783 has B band archival observations only in the F435W filter of ACS/WFC. Hence, Saracino et al. (2020) used $C_{F275W,F343N,F435W}$ for NGC 1783 and $C_{F275W,F343N,F438W}$ for Lindsay 1 and NGC 2121.

width lower limits to the actual values. They also note that the effects are more pronounced for young GCs than old/intermediate ones. Hence we may expect an increase in the RGB widths of NGC 2121 and NGC 1783 if the abundance variations due to first dredge-up are accounted for.

5.1.2 Evidence contradicting the role of age

Milone et al. (2020) calculated the fraction of 1G stars in various SMC and LMC clusters including the six SMC clusters and one LMC cluster investigated by Lagioia et al. (2019a). They don't find any significant difference relative to the 1G fractions of Galactic GCs and ages, though they find that the 1G fractions of NGC 339 and NGC 1978 are significantly higher than those of Galactic GCs. This is corroborated by Dondoglio et al. (2021) who find no correlation between the 1G fractions of GCs hosting MPs and their ages. But, as stated by Milone et al. (2020), no strong conclusion can be drawn from these findings since direct comparison of the values of Galactic GCs and MC GCs is rendered difficult owing to their different masses and ages. Figure 5.3 shows the relationship between age and 1G fraction (N_{1G}/N_{TOT}) of MC GCs (blue circles) and Galactic GCs (red and grey circles) as determined by Milone et al. (2020).

5.2 Effect of host galaxy on MPs

5.2.1 Evidence suggesting the role of host galaxy

Milone et al. (2017) and Marino et al. (2019) classify GCs into two types - Type I and Type II - based on the ChMs of 58 GCs. Type I GCs are those which exhibit only a single sequence of 1G and 2G populations while Type II GCs exhibit multiple sequences of 1G and 2G populations with star-to-star variations in heavy elements like Fe and s-process elements. The ratio of the number of Type I and Type II GCs is 5:1. There are totally 13 known Type II GCs. Massari et al. (2019) and Milone et al. (2020) find that six (or possibly seven) of these clusters are found in two specific regions of the integrals of motion (IOM) space and hence conclude that these clusters are possibly associated with the same parent galaxy, likely to be *Gaia*-Enceladus. Figure 5.4 shows the IOM space for Galactic GCs defined by the angular momentum component in the z direction (L_z) and the angular momentum component perpendicular to L_z (L_{PERP}). Milone et al. (2020) concludes

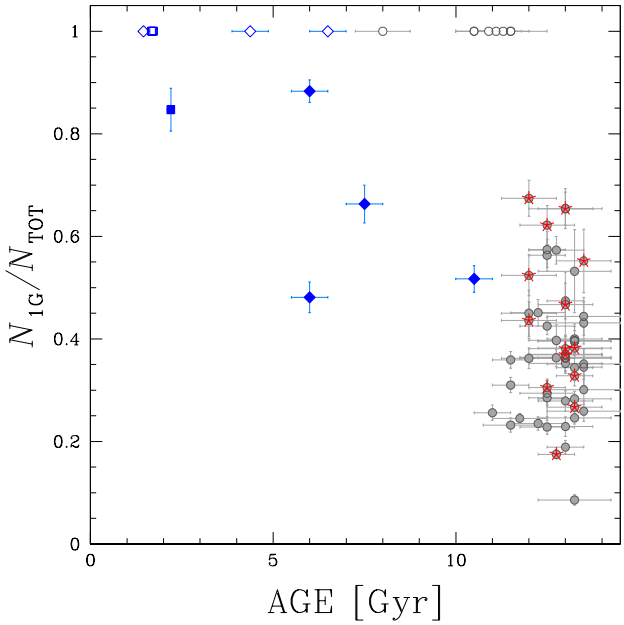

Figure 5.3: Age vs N_{1G}/N_{TOT} for MC and Galactic GCs. MC GCs are indicated by blue circles. Galactic GCs with a perigaalctic radius less than and greater than 3.5 kpc are indicated by grey and red cicles respectively. Circles with $N_{1G}/N_{TOT} = 1$ are GCs without evidence of MPs. Figure adapted from Milone et al. (2020).

that since Type II GCs are not found in Magellanic Clouds and six of the known Galatic Type II GCs are associated with a single parent galaxy, their formation is possibly dependent on their host galaxy.

At least four of the 13 known Type II GCs are linked with the main bulge and the main disc component of MW, hence we know Type II GCs are not exclusively of extragalactic origin. Classical MC GCs have similar metallicity spreads as Galactic GCs (Piatti & Koch 2018). The mass of *Gaia*-Enceladus during collision with MW was similar to SMC and based on the abundances of low metallicity stars of LMC, it could have been similar to LMC in its formative years (Helmi et al. 2018; Hayes et al. 2018; van der Marel et al. 2009). The star formation rate of SMC is similar to that of *Gaia*-Enceladus with more than one star formation event. (Rezaeikh et al. 2014; Fernández-Alvar et al. 2018). These similarities between the galaxy environments make it reasonable to think that the apparent absence of Type II GCs in MCs could be due to the relatively lesser knowledge of MCs compared to MW and that Type II GCs could be detected in MCs with

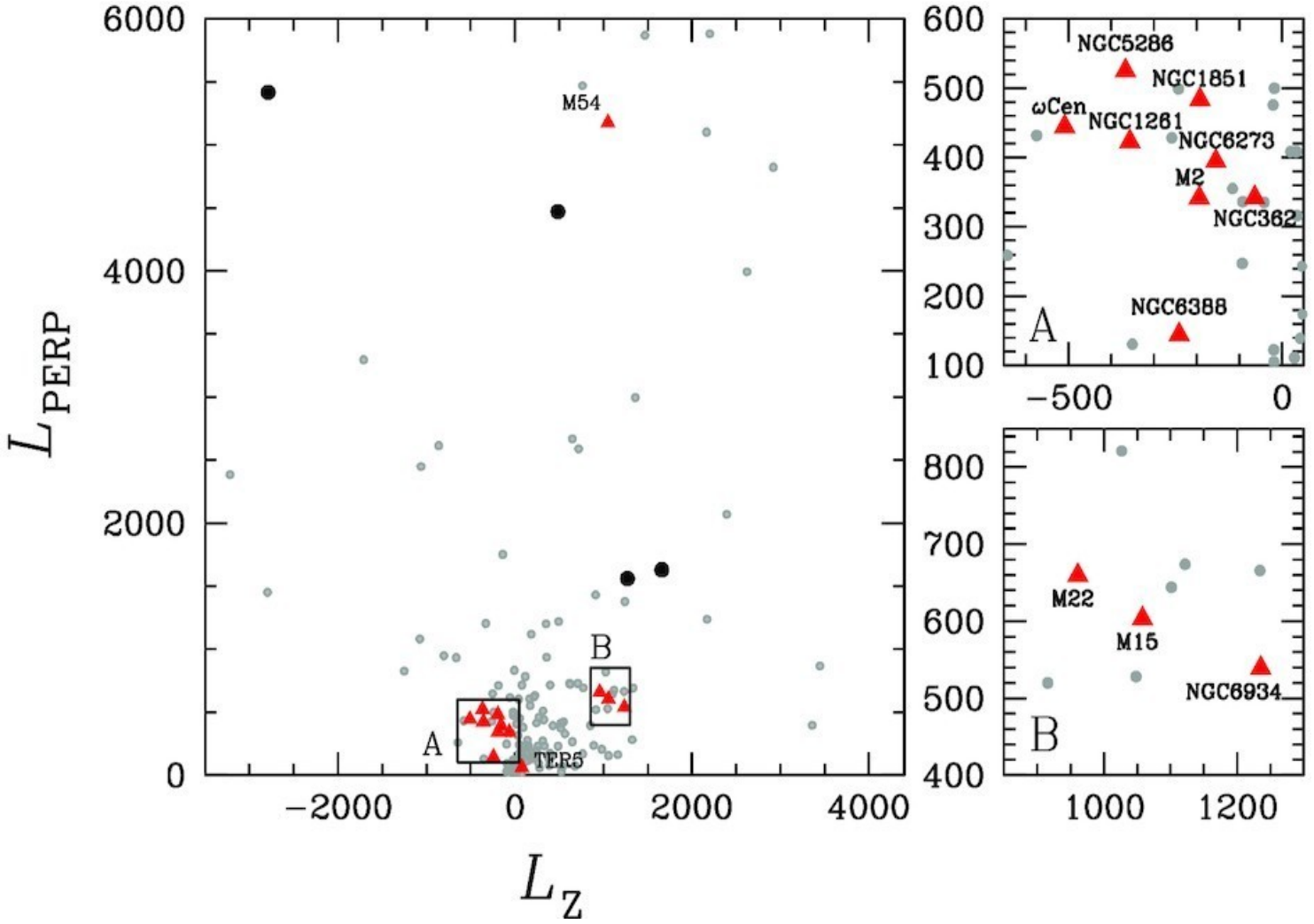

Figure 5.4: IOM space defined by L_z and L_{PERP} for Galactic GCs with Type II clusters indicated by red triangles and SSP candidates indicated by light black circles. We can see that the Type II GCs are clustered in two distinct regions (A and B) of the IOM space. Figure adapted from Milone et al. (2020).

further exploration. The environment of *Gaia*-Enceladus could have been relatively more favourable for the formation of Type II GCs, given that 6 of the 13 known Type II GCs are linked to it. But it may not have played a dominant role in the origin and manifestation of MPs since the incidence of Type I GCs is far greater than that of Type II GCs.

We plotted $\mathrm{Log}(M_c/M_\odot)$ vs $W_{CF336W,F438W,F814W}$ and $\Delta W_{CF336W,F438W,F814W}$ of Galactic GCs shape-coded for the type of GCs, as illustrated in Figure 5.5 and the progenitor of GCs, as illustrated in Figure 5.6 (see Table 1 in Massari et al. 2019). Massari et al. (2019) found 36 GCs unassociated with any of the known progenitor galaxies. 25 of those GCs have low binding energy and are clustered in the IOM space. Hence, those GCs are hypothesized to have originally been part of a single low energy galaxy termed as 'Low Energy Progenitor'. The remaining 11 GCs have high binding energy and were scattered in the IOM space. Hence they are considered to have different origins but labelled as 'High Energy Progenitor' for convenience. Figure 5.5 neither shows any significant difference between the trends traced by Type I and Type II GCs nor by Type II GCs of different progenitors. The trend is replicated when we replace M_c with M_{ini}, MLF, MLA and ML as illustrated in Figures B.1, B.3, B.5 and B.7 respectively. Top panel of Figure 5.6 shows that *in-situ* Galactic GCs systematically have higher $W_{CF336W,F438W,F814W}$ with higher [Fe/H] but the difference vanishes once the effect of [Fe/H] is subtracted, as shown in the lower panel of Figure 5.6. This trend is also replicated when we replace M_c with M_{ini}, MLF, MLA and ML as illustrated in Figures B.2, B.4, B.6 and B.8 respectively. This corroborates our finding that galaxy environment may not play a dominant role in the origin and manifestation of MPs.

5.2.2 Evidence contradicting the role of host galaxy

Saracino et al. (2019) investigated Lindsay 1 using ChM in $\Delta C_{F275W,F336W,F438W}$ pseudo-colour and $m_{F275W} - m_{F814W}$ colour and compared it with the Galactic GC NGC 288. Lindsay 1 and NGC 288 have similar metallicities but belong to different age ranges and galactic environments. They observe that the 1G and the 2G populations have similar separations (see panel (a) in Figure 5.7) and their Helium enrichments are also similar (Chantereau et al. 2019; Milone et al. 2018). Hence, they conclude that the phenomenon of MPs is independent of age and galaxy environment. Panel (b) in Figure 5.7 compares the positions of Lindsay 1 and NGC 288 stars in $m_{F275W} -$

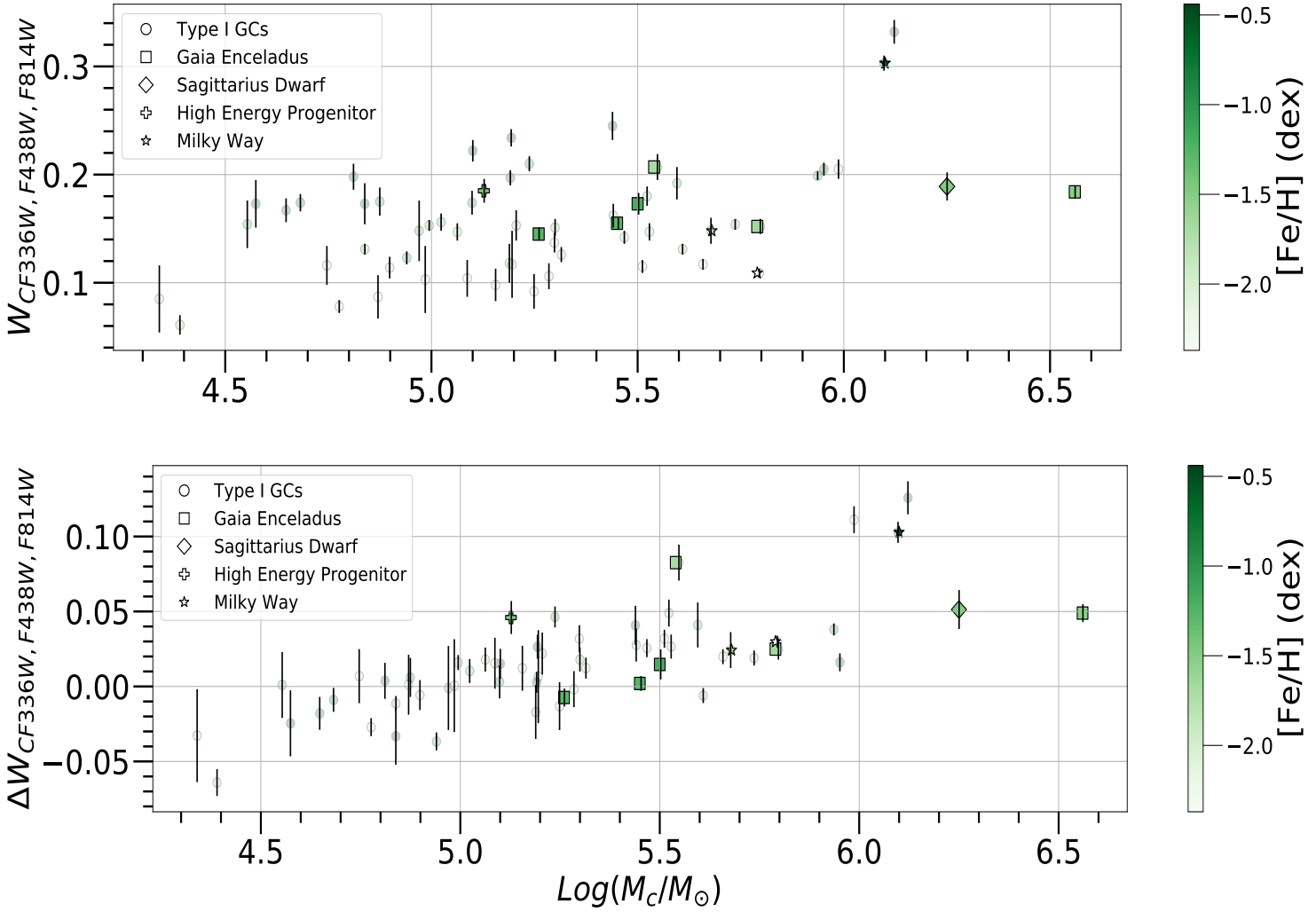

Figure 5.5: Log($M_c/M_\odot$) vs $W_{CF336W,F438W,F814W}$ and $\Delta W_{CF336W,F438W,F814W}$ for the Galactic GCs based on their type and progenitor. Different non-circular symbols represent different progenitors of Type II GCs.

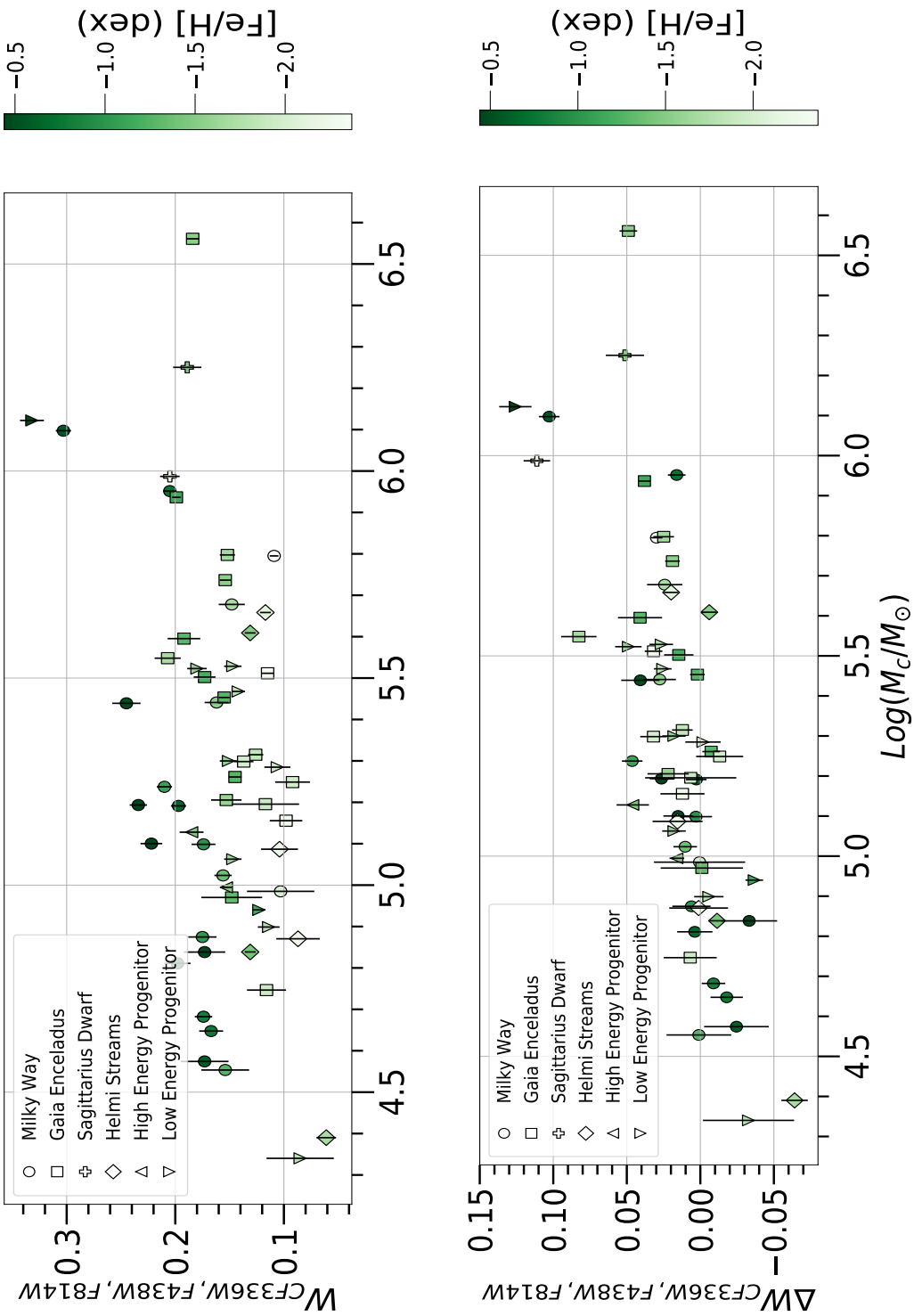

Figure 5.6: $\mathrm{Log}(M_c/M_\odot)$ vs $W_{CF336W,F438W,F814W}$ and $\Delta W_{CF336W,F438W,F814W}$ for the Galactic GCs based on their progenitor. Different symbols represent different progenitors.

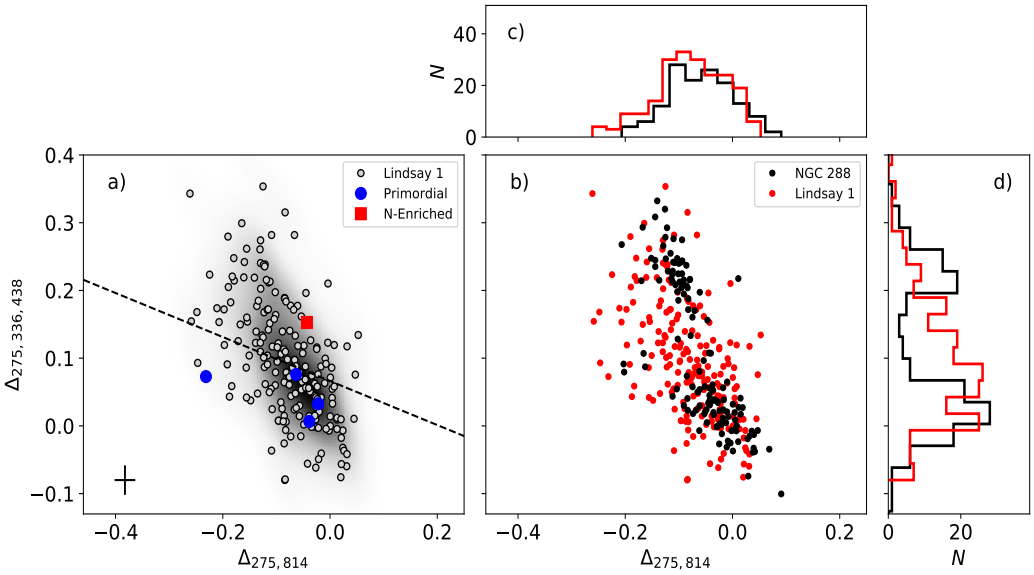

Figure 5.7: Comparison of Lindsay 1 and NGC 288 using $m_{F275W} - m_{F814W}$ vs $\Delta C_{F275W,F336W,F438W}$ ChM. Panel (a) shows that 1G (primordial stars marked in blue circles) and 2G (N-enriched star marked in red square) populations. The black dashed line indicates the separation of 1G and 2G populations of NGC 288 indicating that the population separations between the two clusters are similar. Panel (b) shows the position of Lindsay 1 and NGC 288 stars in the ChM while panels (c) and (d) shows the distributions of $m_{F275W} - m_{F814W}$ and $\Delta C_{F275W,F336W,F438W}$ respectively. Figure adapted from Saracino et al. (2019).

m_{F814W} vs $\Delta C_{F275W,F336W,F438W}$ plane. We can see that their distributions show resemblance, as shown in panels (c) and (d). If this is true, the apparent increase in $\Delta W_{CF336W,F438W,F814W}$ of MC clusters with age in Figure 4.5 may disappear with an increased sample of MC GCs in F336W, F438W and F814W filters.

Chapter 6

Conclusion

6.1 Summary

Research over the last few decades has made it abundantly clear that globular clusters consist of multiple stellar populations rather than simple stellar populations, thanks to advanced instrumentation. But the origin of MPs remains unclear. One aspect of the problem is to determine whether the galaxy environment plays a role in the formation of MPs. We compared GCs from MW and LMC in the same age range to investigate if their RGB widths show any systematic variations from each other. To that extent, we analyzed two classical LMC GCs namely, NGC 1786 and NGC 1898 and compared them with the available data on classical Galactic GCs. We used DOLPHOT to perform PSF photometry on the clusters, followed by selecting the stars from the photometry output by placing a few quality cuts, statistically removing the field stars and selecting only those stars that lie along the fiducial line of the cluster. The observed RGB width was then determined followed by estimating the uncertainty using bootstrapping and subtracting the photometric error using ASs test to get the intrinsic RGB width. As Lagioia et al. (2019a) found a strong monotonic correlation between the intrinsic RGB width and metallicity, the effect of metallicity was subtracted by computing a linear relation for those clusters with $\mathrm{Log}(M_c/M_\odot) < 5.22$ since they showed adequate linearity. The results showed that significant and strong monotonic correlations arise between the metallicity subtracted RGB width and the total mass of the cluster. So we followed the same method and computed the normalized RGB width and plotted it against the mass parameters listed in Table 3.1 of the two analyzed clusters in addition to the

cluster database used by Lagioia et al. (2019a). We find that NGC 1786 and NGC 1898 follow the upper end of the general trend exhibited by Galactic GCs. We also find that Galactic GCs from different progenitors follow the same general trend as one another. This thesis provides first evidence from an analysis of a large sample of GCs that galaxy environment may not play a dominant role in the formation of MPs.

6.2 Future prospects

Though this thesis may have given evidence that the galaxy environment may have played only a minor role, there are quite a few caveats. To explore the role of age and its possible dependence on the correlations we have observed between RGB width and mass-based parameters, we need to analyze a large sample of GCs hosting MPs across various age ranges in the same galactic environment. Magellanic Clouds may serve as the perfect system to resolve this question since we have detected MPs in GCs as young as 1.5 Gyr and as old as 10 Gyr. Galactic GCs hosting MPs are classical while the sample of MC GCs used in this thesis, though spanning a wide age range, is too small to derive any reasonably strong conclusions. The studies discussed in Section 5.1 also have an extremely small sample. There is also a need for a much larger sample of classical LMC GCs in the filter combination used in this thesis and that of Martocchia et al. (2019) and Saracino et al. (2020) to verify our results and also explore the role of metallicity, mass and age in formation of MPs in greater detail.

In Section 5.2.1, we have compared Galactic GCs based on their progenitors and concluded that there are no noticeable trends unique to any specific progenitor. But there is an open question as to whether GCs undergo change after they accrete onto another galaxy. Miholics et al. (2016) performed N-body simulations of star clusters to study as to how the cluster evolves due to change in potential during and after dwarf galaxy mergers with MW. They find that once the influence of the dwarf galaxy diminishes and the cluster comes under MW influence, the cluster shrinks and becomes the same size as a cluster formed within MW on the same orbit. So, to truly determine the role of the galaxy environment, we need to compare GCs that inhabit the galactic environments they were formed in.

New developments in instrumentation also promise more insights in the near future. Particularly, the Near Infrared Camera (NIRCam) and Near Infrared Spectrograph onboard James Webb Space Telescope (JWST) will

extend the distance limit within which we can detect GCs with MPs (Salaris et al. 2019). We already know that MPs have been detected in the MS stars from HST NIR studies (Milone et al. 2012c, 2019; Dondoglio et al. 2022). At the time of writing this thesis, one General Observer program (GO-2560, PI: Anna Marino) and one Early Release Science program (ERS-1334, PI: Daniel Weisz) for JWST have been approved to study stellar populations in the NIR with the GO program specifically targeted to study MPs in M-dwarfs. Very low mass (< 0.4 M$\odot$) stars like M-dwarfs have lower effective temperature and peak spectrally in the infrared region making them suitable targets for JWST. Nardiello et al. (2022) detected MPs in the Galactic GC M92 using JWST CMDs (data from ERS-1334), the first JWST CMDs of a GC. Based on the synthetic studies of Salaris et al. (2019) to determine the optimal NIRCam filters to detect MPs, Milone et al. (2023) studied 47 Tuc using JWST NIRCam (data from GO-2560), WFC3/NIR and WFC/ACS cameras and detected MPs with three 2G sequences. A JWST proposal aiming to study proto-GCs at high redshifts has also been approved (GO-1635, PI: Crystal Martin), giving us opportunities to potentially study the formation and early environment of GCs which is necessary to understand the formation of MPs.

Appendix A

Normalized RGB width vs mass parameters

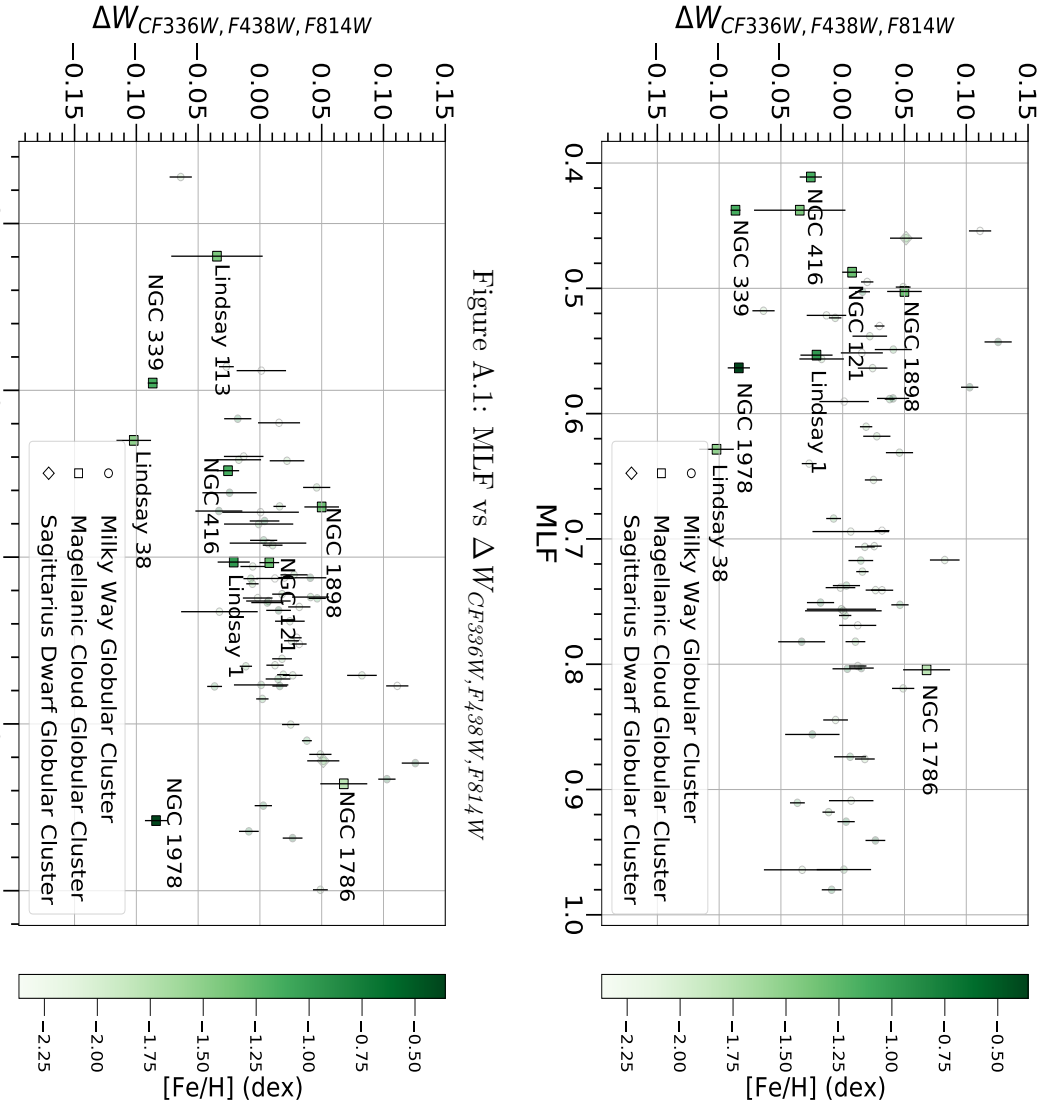

Figure A.1: MLF vs $\Delta W_{CF336W,F438W,F814W}$

Figure A.2: Log(MLA) vs $\Delta W_{CF336W,F438W,F814W}$

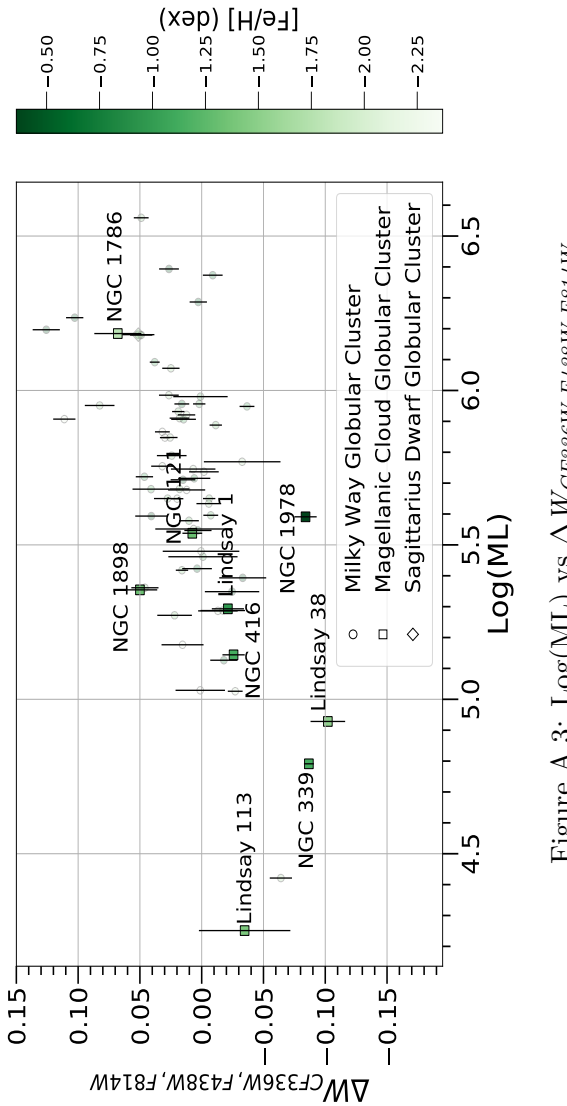

Figure A.3: Log(ML) vs $\Delta W_{CF336W,F438W,F814W}$

Appendix B

Normalized RGB width vs mass parameters for Galactic GCs of different types and progenitors

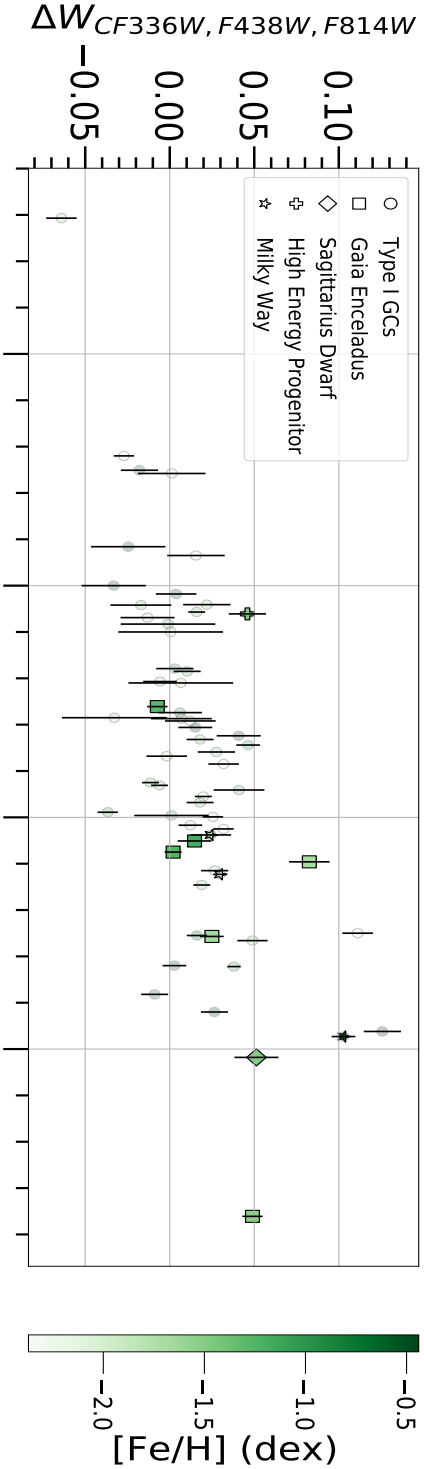

Figure B.1: $\mathrm{Log}(M_{ini}/M_\odot)$ vs $\Delta\, W_{CF336W,F438W,F814W}$ for the Galactic GCs based on their type and progenitor. Different non-circular symbols represent different progenitors of Type II GCs.

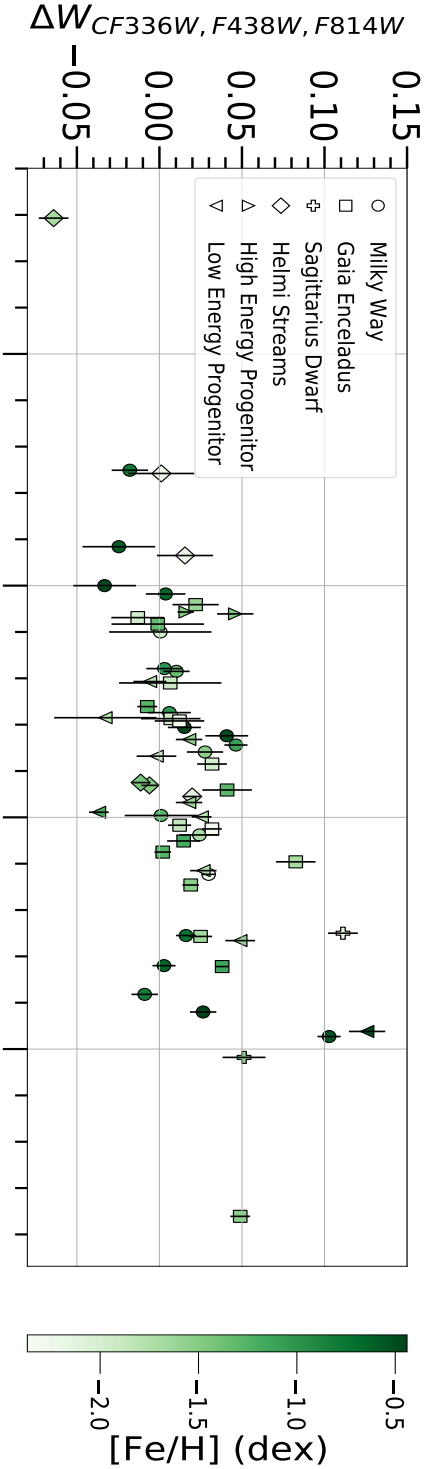

Figure B.2: $\mathrm{Log}(M_{ini}/M_\odot)$ vs $\Delta\, W_{CF336W,F438W,F814W}$ for the Galactic GCs based on their progenitor. Different symbols represent different progenitors.

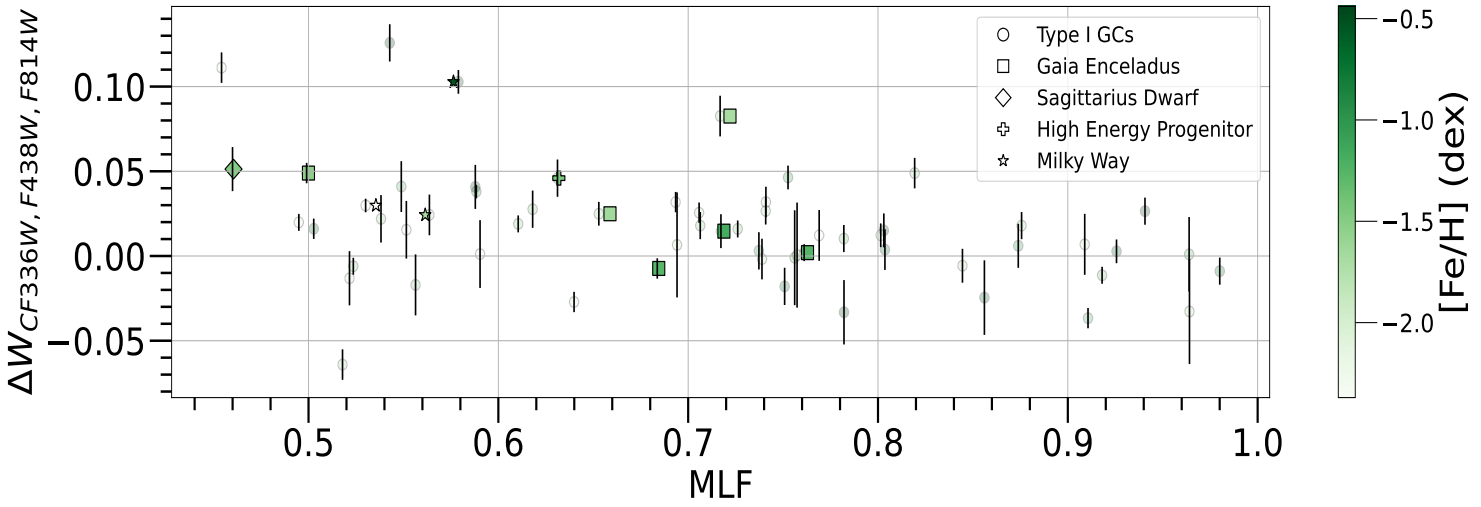

Figure B.3: Same as Figure B.1 but with MLF.

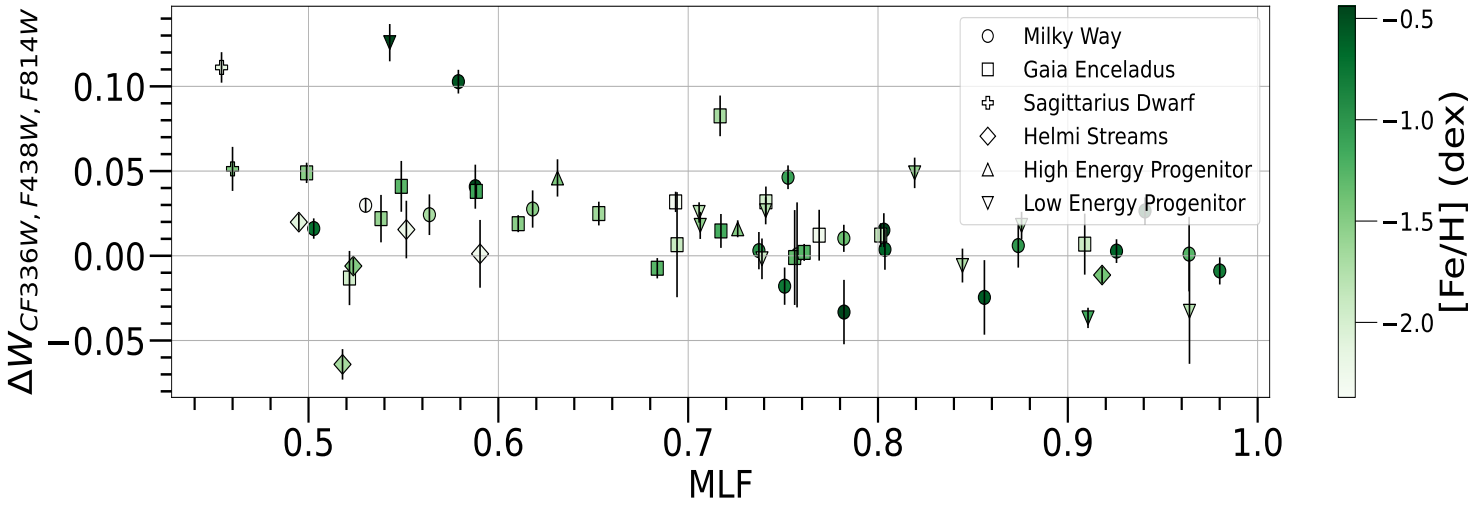

Figure B.4: Same as Figure B.2 but with MLF.

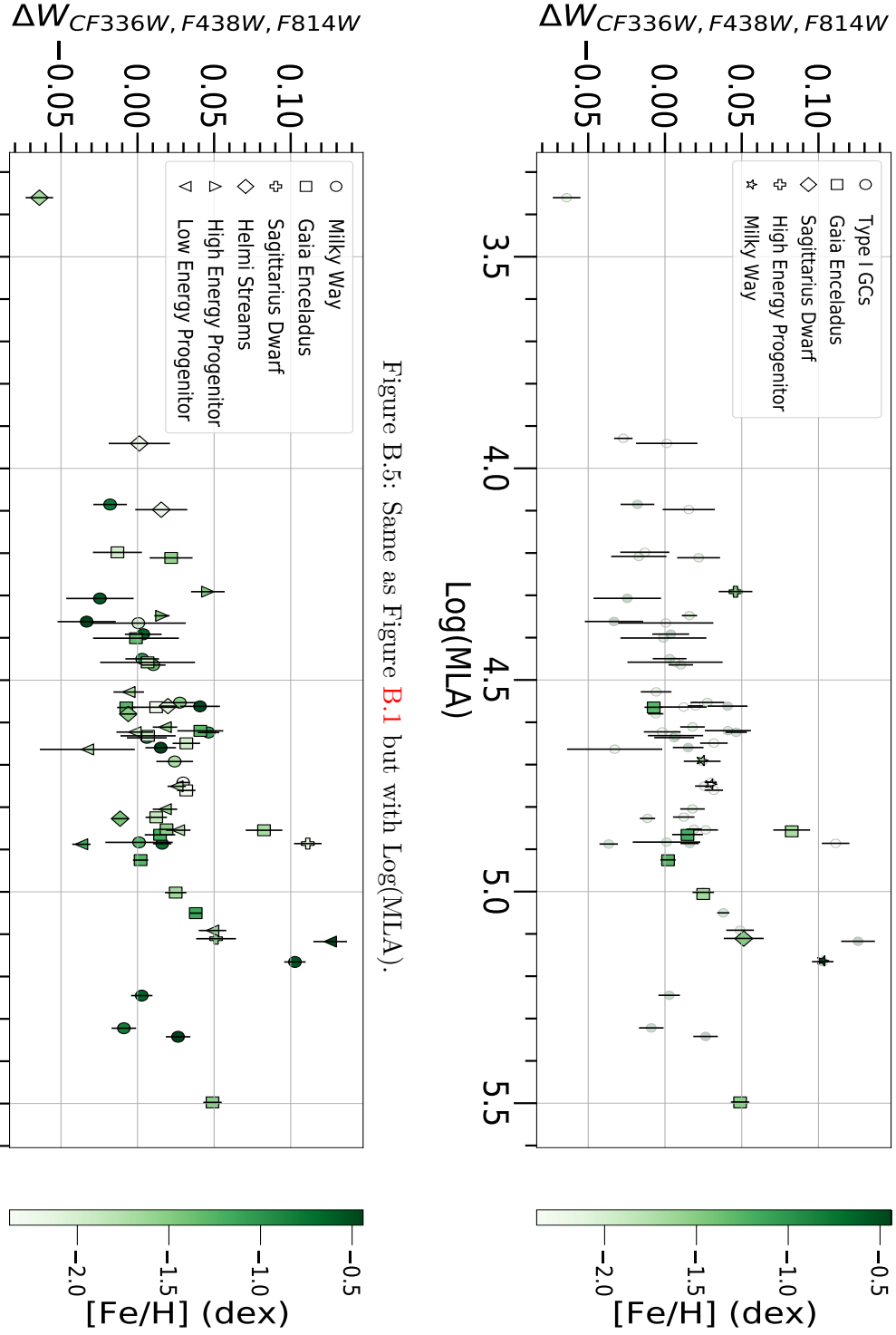

Figure B.5: Same as Figure B.1 but with Log(MLA).

Figure B.6: Same as Figure B.2 but with Log(MLA).

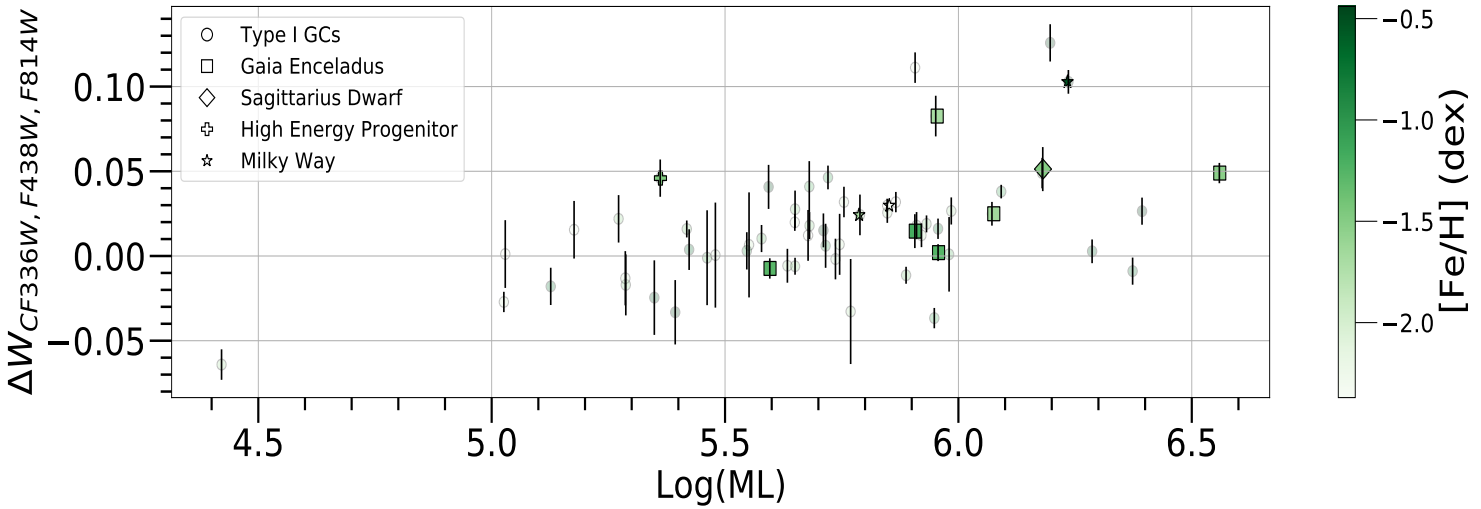

Figure B.7: Same as Figure B.1 but with Log(ML).

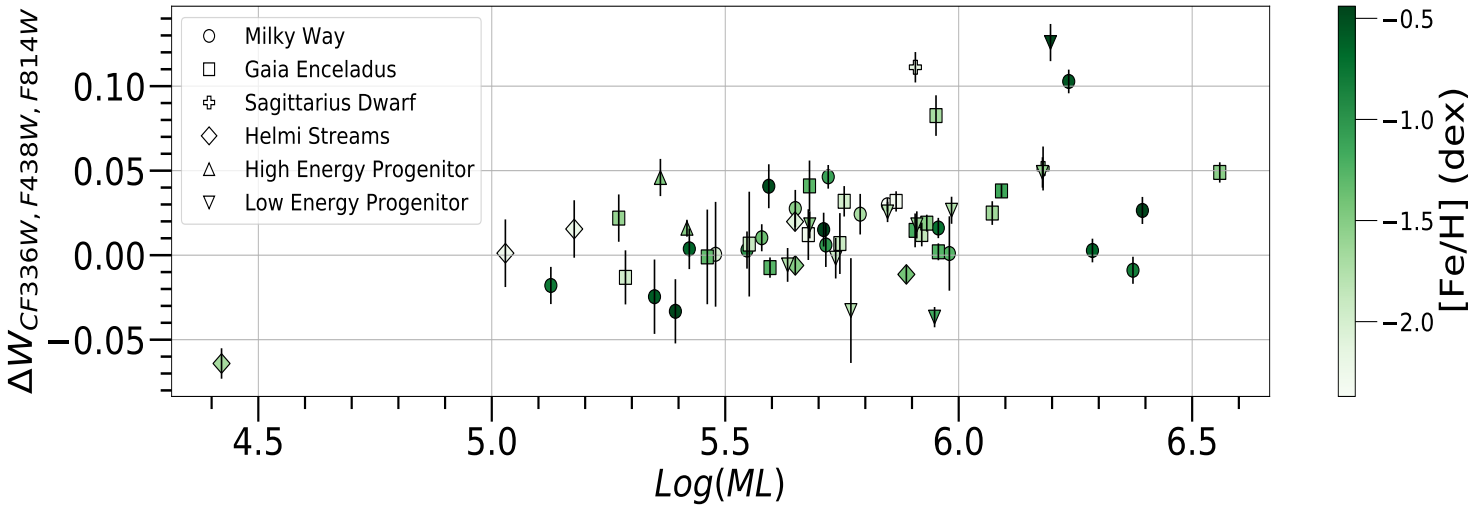

Figure B.8: Same as Figure B.2 but with Log(ML).

Bibliography

Anderson J., King I. R., 2000, PASP, 112, 1360

Anderson J., et al., 2008, AJ, 135, 2055

Baggett S., Gosmeyer C., Noeske K., 2015, WFC3/UVIS Charge Transfer Efficiency 2009-2015, Instrument Science Report WFC3 2015-003, 15 pages

Bastian N., Lardo C., 2018, ARAA, 56, 83

Bastian N., Lamers H. J. G. L. M., de Mink S. E., Longmore S. N., Goodwin S. P., Gieles M., 2013, MNRAS, 436, 2398

Baumgardt H., Hilker M., 2018, MNRAS, 478, 1520

Baumgardt H., Hilker M., Sollima A., Bellini A., 2019, MNRAS, 482, 5138

Beasley M. A., Hoyle F., Sharples R. M., 2002, MNRAS, 336, 168

Bellini A., Anderson J., Salaris M., Cassisi S., Bedin L. R., Piotto G., Bergeron P., 2013, ApJ, 769, L32

Cadelano M., Dalessandro E., Salaris M., Bastian N., Mucciarelli A., Saracino S., Martocchia S., Cabrera-Ziri I., 2022, ApJ, 924, L2

Carretta E., et al., 2009, A&A, 505, 117

Carretta E., et al., 2015, A&A, 578, A116

Chantereau W., Salaris M., Bastian N., Martocchia S., 2019, MNRAS, 484, 5236

D'Antona F., Vesperini E., D'Ercole A., Ventura P., Milone A. P., Marino A. F., Tailo M., 2016a, MNRAS, 458, 2122

D'Antona F., Vesperini E., D'Ercole A., Ventura P., Milone A. P., Marino A. F., Tailo M., 2016b, MNRAS, 458, 2122

Dalessandro E., Lapenna E., Mucciarelli A., Origlia L., Ferraro F. R., Lanzoni B., 2016, ApJ, 829, 77

Dantona F., Gratton R., Chieffi A., 1983, Mem. Della Soc. Astron. Ital., 54, 173

Decressin T., Meynet G., Charbonnel C., Prantzos N., Ekström S., 2007, A&A, 464, 1029

Deustua S. E., Mack J., 2018, Comparing the ACS/WFC and WFC3/UVIS Calibration and Photometry, Space Telescope WFC Instrument Science Report

Di Stefano R., Ray A., 2016, ApJ, 827, 54

Dolphin A. E., 2000, PASP, 112, 1383

Dondoglio E., Milone A. P., Lagioia E. P., Marino A. F., Tailo M., Cordoni G., Jang S., Carlos M., 2021, ApJ, 906, 76

Dondoglio E., et al., 2022, ApJ, 927, 207

Dotter A., 2016, ApJS, 222, 8

Dotter A., et al., 2010, ApJ, 708, 698

Dotter A., Sarajedini A., Anderson J., 2011, ApJ, 738, 74

Dotter A., Milone A. P., Conroy C., Marino A. F., Sarajedini A., 2018, ApJ, 865, L10

Elmegreen B. G., 2017, ApJ, 836, 80

Fernández-Alvar E., et al., 2018, ApJ, 852, 50

Fruchter A. S., Hook R. N., 2002, PASP, 114, 144

Gaia Collaboration et al., 2021, A&A, 649, A1

Gilligan C. K., et al., 2019, MNRAS, 486, 5581

Glatt K., et al., 2008, AJ, 136, 1703

Glatt K., et al., 2011, AJ, 142, 36

Goudfrooij P., Puzia T. H., Chandar R., Kozhurina-Platais V., 2011, ApJ, 737, 4

Goudfrooij P., et al., 2014, ApJ, 797, 35

Harris W. E., 1996, AJ, 112, 1487

Hayes C. R., et al., 2018, ApJ, 852, 49

Heasley J. N., 1999, in Craine E. R., Crawford D. L., Tucker R. A., eds, Astronomical Society of the Pacific Conference Series Vol. 189, Precision CCD Photometry. p. 56

Helmi A., Babusiaux C., Koppelman H. H., Massari D., Veljanoski J., Brown A. G. A., 2018, Nature, 563, 85

Herschel W., 1789, Philosophical Transactions of the Royal Society of London Series I, 79, 212

Hollyhead K., et al., 2017, MNRAS, 465, L39

Hook R., Stoehr F., 2008, WFC3 Support in Tiny Tim, Instrument Science Report WFC3 2008-014, 14 pages

Jarvis M., Jain B., 2004, arXiv e-prints, pp astro–ph/0412234

Johnson J. A., Ivans I. I., Stetson P. B., 2006, ApJ, 640, 801

Krist J., 1993, in Hanisch R. J., Brissenden R. J. V., Barnes J., eds, Astronomical Society of the Pacific Conference Series Vol. 52, Astronomical Data Analysis Software and Systems II. p. 536

Krist J. E., Hook R. N., Stoehr F., 2011, in Kahan M. A., ed., Society of Photo-Optical Instrumentation Engineers (SPIE) Conference Series Vol. 8127, Optical Modeling and Performance Predictions V. p. 81270J, doi:10.1117/12.892762

Lagioia E. P., et al., 2018, MNRAS, 475, 4088

Lagioia E. P., Milone A. P., Marino A. F., Cordoni G., Tailo M., 2019a, AJ, 158, 202

Lagioia E. P., Milone A. P., Marino A. F., Dotter A., 2019b, ApJ, 871, 140

Larsen S. S., Brodie J. P., Grundahl F., Strader J., 2014, ApJ, 797, 15

Leauthaud A., et al., 2007, ApJS, 172, 219

Lee Y. W., Joo J. M., Sohn Y. J., Rey S. C., Lee H. C., Walker A. R., 1999, Nature, 402, 55

Lindblad B., 1922, ApJ, 55, 85

Longmore S. N., 2015, MNRAS, 448, L62

Madau P., Dickinson M., 2014, ARAA, 52, 415

Marino A. F., Villanova S., Piotto G., Milone A. P., Momany Y., Bedin L. R., Medling A. M., 2008, A&A, 490, 625

Marino A. F., et al., 2015, MNRAS, 450, 815

Marino A. F., et al., 2019, MNRAS, 487, 3815

Martocchia S., et al., 2018a, MNRAS, 473, 2688

Martocchia S., et al., 2018b, MNRAS, 477, 4696

Martocchia S., et al., 2019, MNRAS, 487, 5324

Massari D., Koppelman H. H., Helmi A., 2019, A&A, 630, L4

McLaughlin D. E., van der Marel R. P., 2005, ApJS, 161, 304

Miholics M., Webb J. J., Sills A., 2016, MNRAS, 456, 240

Milone A. P., Marino A. F., 2022, Universe, 8, 359

Milone A. P., Bedin L. R., Piotto G., Anderson J., 2009, A&A, 497, 755

Milone A. P., et al., 2012a, A&A, 540, A16

Milone A. P., et al., 2012b, ApJ, 744, 58

Milone A. P., et al., 2012c, ApJ, 754, L34

Milone A. P., et al., 2013, ApJ, 767, 120

Milone A. P., et al., 2014, ApJ, 785, 21

Milone A. P., et al., 2015, ApJ, 808, 51

Milone A. P., et al., 2017, MNRAS, 464, 3636

Milone A. P., et al., 2018, MNRAS, 481, 5098

Milone A. P., et al., 2019, MNRAS, 484, 4046

Milone A. P., et al., 2020, MNRAS, 491, 515

Milone A. P., et al., 2023, arXiv e-prints, p. arXiv:2301.10889

Mucciarelli A., Origlia L., Ferraro F. R., Pancino E., 2009, ApJ, 695, L134

Nardiello D., Bedin L. R., Burgasser A., Salaris M., Cassisi S., Griggio M., Scalco M., 2022, MNRAS, 517, 484

Niederhofer F., Hilker M., Bastian N., Silva-Villa E., 2015, A&A, 575, A62

Niederhofer F., et al., 2017a, MNRAS, 464, 94

Niederhofer F., et al., 2017b, MNRAS, 465, 4159

Olszewski E. W., Schommer R. A., Suntzeff N. B., Harris H. C., 1991, AJ, 101, 515

Piatti A. E., Koch A., 2018, ApJ, 867, 8

Pietrinferni A., Cassisi S., Salaris M., Percival S., Ferguson J. W., 2009, ApJ, 697, 275

Piotto G., et al., 2015, AJ, 149, 91

Popper D. M., 1947, ApJ, 105, 204

Rezaeikh S., Javadi A., Khosroshahi H., van Loon J. T., 2014, MNRAS, 445, 2214

Salaris M., 2013, in European Physical Journal Web of Conferences. p. 02002, doi:10.1051/epjconf/20134302002

Salaris M., Cassisi S., Mucciarelli A., Nardiello D., 2019, A&A, 629, A40

Salaris M., et al., 2020, MNRAS, 492, 3459

Salinas R., Strader J., 2015, ApJ, 809, 169

Saracino S., et al., 2019, MNRAS, 489, L97

Saracino S., et al., 2020, MNRAS, 493, 6060

Silverman B., 1986, Monographs on Statistics and Applied Probability. Springer

Smith G. H., Briley M. M., 2006, PASP, 118, 740

Valcin D., Bernal J. L., Jimenez R., Verde L., Wandelt B. D., 2020, JCAP, 2020, 002

Valcin D., Jimenez R., Verde L., Bernal J. L., Wandelt B. D., 2021, JCAP, 2021, 017

Vanaraj V., Niederhofer F., Goudfrooij P., 2021, MNRAS, 507, 282

VandenBerg D. A., Brogaard K., Leaman R., Casagrande L., 2013, ApJ, 775, 134

Ventura P., D'Antona F., Mazzitelli I., Gratton R., 2001, ApJ, 550, L65

Whitmore B. C., Zhang Q., Leitherer C., Fall S. M., Schweizer F., Miller B. W., 1999, AJ, 118, 1551

Yong D., Grundahl F., Johnson J. A., Asplund M., 2008, ApJ, 684, 1159

Yong D., et al., 2013, MNRAS, 434, 3542

Zennaro M., Milone A. P., Marino A. F., Cordoni G., Lagioia E. P., Tailo M., 2019, MNRAS, 487, 3239

de Mink S. E., Pols O. R., Langer N., Izzard R. G., 2009, A&A, 507, L1

van Dokkum P. G., et al., 2008, ApJ, 677, L5

van der Marel R. P., Kallivayalil N., Besla G., 2009, in Van Loon J. T., Oliveira J. M., eds, Vol. 256, The Magellanic System: Stars, Gas, and Galaxies. pp 81–92 (arXiv:0809.4268), doi:10.1017/S1743921308028299